Nanoscale

ROYAL SOCIETY OF CHEMISTRY

REVIEW

View Article Online
View Journal | View Issue

Cite this: *Nanoscale*, 2024, **16**, 9235

Self-powered photodetectors: a device engineering perspective

Varun Goel, [a] Yogesh Kumar, [a] Gopal Rawat [b] and Hemant Kumar *[a]

Received 10th February 2024,
Accepted 7th April 2024

DOI: 10.1039/d4nr00607k

rsc.li/nanoscale

Nanoscale self-powered photodetectors that can work without any external source of energy are required for future applications. There is potential demand for these devices in areas like wireless surveillance, weather forecasting, remote monitoring, and places where the availability of power is scarce. This study provides an overview of state of the art research trends and improvements in self-powered photodetectors. A device engineering perspective for improvement in the figures of merit has been presented along with a description of additional effects like pyro-phototronic, piezo-phototronic, and surface plasmonics.

1 Introduction

Currently, sensor-based systems are needed to pave the way for future technologies, primarily in the domain of automation and miniaturization. One of the fundamental units of sensors for technology enhancement is a photodetector. The range of applications for photodetectors covers a wide domain, including:

- *Monitoring of agricultural and forest lands*:[1] photodetectors are mounted on a satellite or a drone, positioned above the land. Light of different wavelengths (for example red, green, blue, near-infrared (NIR) region) is incident on the land. The light reflected from the surface of the land, which in turn depends on the surface characteristics, is sensed by the photodetector. Data from the photodetector are continuously sent to the ground station or processing center where they are analyzed. The information can be used to monitor crop growth, detect changes in vegetation health, and detect changes in land cover.
- *Wireless capsule endoscopy*:[2] a photodetector array is typically used as an endoscopic camera with a wireless capsule to

[a]*Department of Electronics and Communication Engineering, Jaypee Institute of Information Technology, Noida, India. E-mail: varun.goel@jiit.ac.in, yogesh.kumar@jiit.ac.in, hemant.kumar@jiit.ac.in*
[b]*School of Computing and Electrical Engineering, Indian Institute of Technology, Mandi, India. E-mail: gopal@iitmandi.ac.in*

Varun Goel

Varun Goel received his B.Tech degree from Uttar Pradesh Technical University, Lucknow, in 2011 and his M.Tech degree from the Indian Institute of Technology (BHU), Varanasi, with a specialization in microelectronics in 2014. Recently, he completed his Ph.D. at the Jaypee Institute of Information Technology, Noida. His research area includes the fabrication and characterization of quantum dot-based thin-film sensors. He has published 13 articles, of which 3 articles are based on self-powered photodetectors and have been published in IEEE Transactions of Electron Devices and IEEE Photonics Technology Letters.

Yogesh Kumar

Yogesh Kumar received a B.E. degree in Electronics and Instrumentation Engineering from Samrat Ashok Technological Institute (SATI) Vidisha, India, in 2009, and M. Tech. and Ph.D. degrees in Microelectronics Engineering from the Department of Electronics Engineering, IIT (BHU), Varanasi, India, in 2013 and 2018. Currently, he is working as an assistant professor at the Jaypee Institute of Information Technology, Noida U.P. His research interests are in the fabrication and characterization of spectrum selective and band gap tunable ultraviolet photodetectors. He has published articles in around 20 SCI journals, including 13 IEEE journals, and 2 ACS journals.

capture and transmit images from within the body. The photodetector is placed at the end of the wireless endoscope and it reports on the variation in light intensity (or any fluorescence) from the surrounding environment to the external monitor. This allows the operator to visualize the internal body structure and examine the internal organs (or tissues) without any invasive procedures. The requirement for this entire procedure depends upon the quality of the photodetectors used in the wireless capsule endoscope. There are two important factors associated with the photodetector. The first one is that the photodetector should be non-toxic and ideally dissolve within the body (or be excreted), and the second is that the photodetector must work under very low-light conditions and avoid any kind of noise interference for accurate detection.

• *Biomedical*[3] *and diagnostic imaging*:[4] photodetectors are used to detect the X-rays that pass through a patient's body and convert them into electrical signals. An X-ray detector then processes these signals to produce an image of the internal body organs. Another common use of photodetectors in biomedical imaging is optical imaging techniques such as fluorescence imaging and bioluminescence imaging. In these techniques, a photodetector is used to detect the light emitted by fluorescent or bioluminescent molecules, which have been tagged to specific molecules or cells in the body. This enables non-invasive imaging of specific biological processes or structures. In addition, photodetectors are also used in medical ultrasound imaging, which uses high-frequency waves to create images of internal organs, blood vessels, and other structures inside the body.

• *Night vision*:[5] photodetectors are used to detect low levels of light, such as infrared or starlight, to create a visible image for the viewers by utilizing an amplifier. There are several types of photodetectors used in night vision devices, including image intensifier tubes, thermal imaging cameras, and low-light CMOS or CCD sensors.

• *Structural testing*:[6] photodetectors are used to detect and measure subtle changes in the properties of a material or structure, such as surface cracks, internal defects, and variations in thickness or density.

• *Wearable and implantable medical devices*:[7] Photodetectors are used to detect and measure various physiological signals, such as heart rate, blood oxygen levels, and blood pressure. Some of the most common types of photodetectors used in these devices include photoplethysmography (PPG) sensors, which use light-emitting diodes (LEDs) and photodiodes to measure changes in blood volume, which can be used to deter-

Gopal Rawat

Gopal Rawat was born in Uttarakhand, India. For his academic studies, Dr Rawat has earned his B.Tech., M.Tech., and Ph.D. degrees in the years 2011, 2013 and 2018, respectively. He received his M.Tech. and Ph.D. degrees from the Department of Electronics Engineering, IIT (BHU), Varanasi, India, with a specialization in microelectronics engineering. After completing his Ph.D., he joined IIT Mandi, India, as an Assistant Professor and is currently serving as a faculty member in the School of Computing and Electrical Engineering (SCEE). Dr Rawat has broad research interests in semiconductor devices/physics/materials, micro/nano-electronics, etc. *His research interests include semiconductor devices, circuits, and sensing applications. He has published 65+ research articles in leading peer-reviewed international journals like IEEE Transactions, IEEE Letters, Sensors & Actuators, ACS Applied Electronic Materials,* etc *and presented at conferences. He has authored a book chapter and has been credited on 4 patents. He has been granted three patents. Currently, he is investigating five sponsored projects. Dr Rawat has received some prestigious awards and recognition such as BRICS Young Scientist and many more. He is an Advisor for the IEEE Student Branch and IEEE EDS Student Branch Chapter at IIT Mandi. Dr Rawat is a Senior Member of IEEE, USA, and a Lifetime Member of the Institution of Engineers (India) (IEI).*

Hemant Kumar

Hemant Kumar earned his B.E., M.Tech. and Ph.D. degrees from the Rustam Ji Institute of Technology, Gwalior, in 2009; the Indian Institute of Information Technology Gwalior in 2011; and the Indian Institute of Technology (Banaras Hindu University), Varanasi, India, in 2018, respectively. He is currently working as an Assistant Professor in the Department of Electronics Engineering, Jaypee Institute of Information Technology, Noida. His research area includes the fabrication and characterization of quantum dot-based thin film sensors. He has published 25 articles in SCI Journals, including 16 IEEE Journals, and 1 ACS journal.

mine heart rate and blood oxygen levels. Oximeters use LEDs and photodiodes to measure the absorption of light by haemoglobin in the blood, which can be used to determine blood oxygen levels. Photodiodes and phototransistors can be used to determine heart rate, blood pressure, and other physiological signals. Spectrophotometry, which measures the amount of light absorbed or scattered by the tissue, can be used to determine oxygenation, blood flow, and other physiological parameters.

• *Artificial eye mimicking*:[8] Photodetectors detect and process visual information. The artificial retina is a device that mimics the function of the natural eye. It is typically composed of a large array of photodetectors. Photodetectors are typically made of organic or inorganic materials, such as silicon or organic polymers. These artificial retinas can be used to restore vision in people with retinal degenerative diseases, such as retinitis pigmentosa or other age-related macular degeneration, which causes the loss of photoreceptor cells in the retina. The artificial retina can also be used in vision prosthetics for people who have lost their sight due to other causes, such as trauma or cancer.

• *Self-driving vehicles*:[9] Photodetectors are used to detect and interpret visual information from the environment. These photodetectors are typically included in sensor systems, such as cameras, light detection and ranging (LiDAR), and radar, which are used to provide the vehicle with information about its surroundings. Cameras are the most commonly used sensors in self-driving vehicles and they use image sensors, such as CMOS or CCD, to capture visual information. The output of the imager is processed by the vehicle's onboard computer to create a detailed map of the vehicle's surroundings. LiDAR systems use laser beams and photodetectors to measure the distance and shape of objects in the environment and radar uses radio waves to detect objects in the environment. Finally, these sensors work together to provide the vehicle with a detailed understanding of its surroundings, including the location of other vehicles, pedestrians, and obstacles. This information is used by the vehicle's onboard computer to make decisions about how to navigate the environment and avoid collisions.

• *Optical communication*:[10] Photodetectors are an essential component in optical communication systems, which use light to transmit information over long distances. Photodetectors are used in optical receivers that are used to convert the optical signals back into electrical signals for further processing. Some of the most common types of photodetectors used in optical communication include APDs, phototransistors, and photomultipliers (PMT). They are widely used in optical communication systems because of their high sensitivity and fast response time. APDs also have an additional built-in amplification mechanism that increases the sensitivity of the detector. They are used in high-speed and long-distance optical communication systems. Phototransistors use a transistor mechanism to amplify the electrical current generated by the photodiode and are used in optical communication systems that require high sensitivity and low noise. Finally, photomultipliers (PMTs) are used in various optical communication systems, such as fibre-optic, free-space, and satellite systems. The PMT uses a series of photodiodes to amplify the electrical current generated by the first photodiode and is used in systems where extremely high sensitivity is required.

• *Machine vision, image sensing*[4] *and other IoT applications*:[11] photodetectors are also used in machine vision and image sensing applications, which involve the use of cameras and other sensors to capture and interpret visual information.

The primary objective of a photodetector is to discriminate between photons of different wavelengths (energy) of the spectrum. For example, an ideal visible domain imager should be able to accurately differentiate between different shades of colour in the visible spectrum. In a practical approach, three photodetectors sensitive to the red, green, and blue (RGB) regions represent the complete visible domain. The combination of these colours can mimic any colour or wavelength in the visible spectrum. The prospect of utilizing three photodetectors to implement the complete visible spectrum (400 nm to 700 nm) is fascinating and represents one pixel. An array of these pixels is used to visualize the complete image using the imager.[8] The information is generated by the photodetectors in the form of electrical signals, and these signals are reorganized to complete the image, which may be extended to video streams. The entire process of capturing the photons, differentiating their wavelength, and generating an information sequence according to the absorbed photon is a power-hungry process. The photodetectors are consistently put under reverse-bias conditions to reflect the changes in the photocurrent as soon as the detector absorbs the photons. Also, external filter layers are used to recognize the distinction between the photons which in turn reduces the rate of incoming photon flux, thus reducing the sensitivity.[12] These issues limit the application perspective of photodetectors, specifically in the biomedical field,[3] mimicking human eyes,[8] and deploying photodetectors in remote areas for monitoring.[1]

Recently, self-powered photodetectors have become a new area of interest for researchers in the photodetector domain. These photodetectors generate sufficient power on their own for the operation. Hence, they are known as self-powered photodetectors. The development of electric potential due to the photovoltaic effect results in the self-powered phenomenon.[13] The primary objective of the self-powered photodetector is to generate sufficient power for the self-functioning of the photodetector. The working of a self-powered photodetector resembles the working of a solar cell operating in photovoltaic short circuit or open circuit mode[14] but there is a fundamental difference between a self-powered photodetector and a solar cell. Solar cells are meant to absorb the maximum number of photons (irrespective of the photon's wavelength) and convert the same into electricity. In contrast, a self-powered photodetector absorbs photons of the intended wavelength only. The prospects for self-powered photodetectors not only depend upon the power generated by the detector but also on efficiently discriminating between the photons based on energy (or wavelength) given by the spectral selectivity of

the detector. The photodetector is considered spectrum selective if the full-width at half-maxima (FWHM) of the detector is less than 100 nm.[4] Self-powered photodetectors are further classified into two types: one generates sufficient power on its own[15] and the second utilizes an energy harvesting unit.[16] The energy harvesting unit fulfils the power requirement of the photodetector. Focusing on the abovementioned properties of self-powered photodetectors, there is a consistent issue found in the literature with self-powered photodetectors as broadband detectors. Regarding self-powered photodetectors, broadband detectors are closely correlated with the solar cell compared to photodetectors. Thus, this work primarily focuses on self-powered photodetectors, which are spectrum selective. A self-powered photodetector under illumination acts as a light-dependent voltage source (LS) as shown in Fig. 1 and provides sufficient power to trigger the externally dependent circuit or load.

Multiple good review articles are already available in the literature focusing on self-powered photodetectors. Tian *et al.*[17] authored the first state-of-the-art review article on self-powered photodetectors. In this article, the prime focus was on junction engineering only; however, a broad device engineering view was missing. In an article by Ouyang *et al.*,[18] self-powered photodetection was done only using ZnO nanomaterials, which in turn limited sensing to the UV region only. The article by Jayakrishnan[19] discusses one of the latest techniques used in self-powered photodetection *i.e.* ferro-pyro-phototronics. However, there are other techniques that help in improving self-powered photodetector performance metrics like plasmonics, surface passivation and many others. Al Fattah *et al.*[20] discussed UV light sensing only citing junction engineering. Perumal Veeramalai *et al.*[21] focused only on the advantages of a perovskite in self-powered photodetection. The present work is focused on areas that are in general not covered by review articles including the relevance of noise studies for self-powered photodetectors, suitable device engineering techniques to minimize losses, and ways to improve the selectivity and figures of merit of self-powered photodetectors. Section 2 covers noise and performance parameters, followed by material specifications for self-powered photodetectors in section 3. Section 4 focuses on the crucial electric field factor, while section 5 explores the significance of ETLs and HTLs for photodetector performance. Lastly, sections 6–9 explore techniques for enhancing photodetector behaviour, including band-gap engineering, junction engineering, surface passivation, and additional effects.

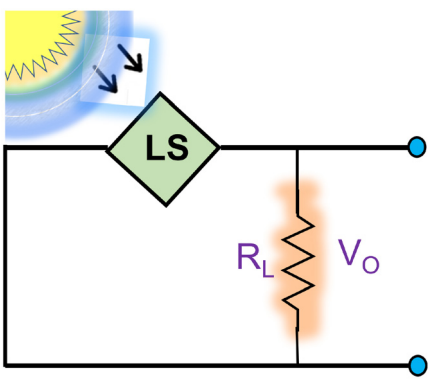

Fig. 1 Self-powered photodetector.

2 Noise and performance parameters

2.1 Sources of noise

The information one can extract from the output of a photodetector is limited by its signal-to-noise ratio (SNR). The signal is the amount of incident photon energy while the noise is the disturbance that results in inaccurate measurement of the signal levels. In order to optimize the conclusion from the response, it is necessary to examine the sources of noise in the photodetector. The details of different sources of noise in the photodetectors are discussed below:

• *Shot noise*: shot noise arises due to the statistically independent nature of photons arriving at the detector.[22] Shot noise is a characteristic of a light source and cannot be eliminated with any technical device. Shot noise is a type of white noise (independent of frequency) and it is directly proportional to the intensity of incident light. The power spectral density of shot noise can be written as:

$$\sigma_{sh}{}^2 = 2qI_{ph} \quad (1)$$

where I_{ph} is the photocurrent.

• *Johnson noise (thermal noise)*: Johnson noise arises from temperature-dependent fluctuations in the load resistor (R_L). It is also a type of white noise. Johnson noise can be represented with the help of a Gaussian distribution with power spectral density can be written as

$$\sigma_{th}{}^2 = \frac{4k_BT}{R_L} \quad (2)$$

where k_B is the Boltzmann constant and T is the temperature. A higher value of the load resistor helps in decreasing thermal noise. However, a higher value of load resistance decreases the bandwidth (inversely proportional to the *RC* value). For high-speed circuits, the typical value of load resistance is 50 Ω.[22]

• *Dark current noise*: an ideal photodetector does not produce any current under dark conditions. However, due to thermal effects, there is still the probability of the spontaneous production of free electrons even in the absence of photons. The dark current has a fixed value at a particular temperature and it decreases with a decrease in temperature. Due to the statistical nature of the carrier generation process, the power spectral density of dark current noise can be written as:

$$\sigma_d{}^2 = 2qI_{dark} \quad (3)$$

The dark current noise and Johnson noise can be reduced by operating the photodetector at a lower temperature.

The other noises associated with photodetectors are flicker noise (1/*f* noise) and technical noise due to various imperfec-

tions. Noise-equivalent-power (NEP) is used to represent the noise power, which is equal to the minimum photon power required to overcome the noise current.[23] It can be calculated from the responsivity per unit bandwidth.[23,24]

$$\text{NEP} = \frac{\sqrt{\langle i_n^2 \rangle}}{\text{responsivity}} \quad (4)$$

where $\langle i_n^2 \rangle$ is the time-averaged square noise power, and NEP is measured in W $\text{Hz}^{-1/2}$.

The study of NEP provides many details about the noise sensitivity of the photodetector. Pal *et al.*[23] studied the noise in a PbS quantum dot (QD)-based p–n junction photodiode. They showed that on increasing the biasing voltage, the EQE of the device increased at a particular wavelength and hence the NEP decreased. However, Lee *et al.*[25] studied the effect of bias on flicker noise. They found that for a bandwidth of 1 kHz, the device (p-GaN/i-ZnO/n-ZnO:Al) exhibited NEPs of 5.56×10^{-12} W and 2.93×10^{-12} W for −5 V and −1 V respectively for 360 nm incident light. Therefore, flicker noise is less significant for self-powered photodetectors. Nawaz *et al.*[26] fabricated a CdS nanobelt-based flexible self-powered photodetector. The detector exhibits a NEP of 2.94×10^{-15} W $\text{Hz}^{-1/2}$. The ultra-low value of NEP is because the dark current of the device is 36 fA under zero-bias conditions. Similarly, Zhang *et al.*[27] fabricated a broadband self-powered photodetector based on $PdSe_2$. They calculated the thermal noise of the device. The thermal noise current is 7.61×10^{-14} A, which is much lower than the dark current (1.54×10^{-11} A) of the device.

2.2 Performance parameters

The concept/process of photodetection involves the following four steps as shown in Fig. 2:

1. *Optical absorption*: it depends on the bandgap of the material and photon energy. Photons will be absorbed if the bandgap of the material is lower than the incident photon energy, otherwise, the semiconductor material (active material) will be transparent to the incident photons. The bandgap of the semiconductor material (E_g) should be lower than the photon energy ($h\nu = hc/\lambda$) to generate e–h pairs. The maximum wavelength (λ) that can generate e–h pairs can be written as:

$$\lambda(\text{nm}) \leq \frac{1242}{E_g(\text{eV})} \quad (5)$$

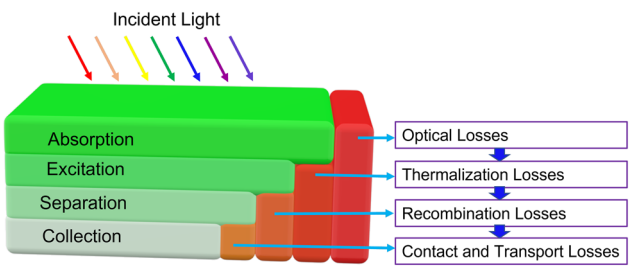

Fig. 2 Photodetection process and associated losses.

where h, ν, and c are Planck's constant, light's frequency, and speed respectively. One can write $hc = 1242 \times 10^{-9}$ eV to minimize the computation complexities.

2. *Charge excitation*: the transfer of energy will happen between absorbed photons and the electrons. This process will excite electrons to the conduction band (higher energy levels), leaving holes in the valence band, thus called photogenerated charge carriers. The generated electrons and holes will undergo a Coulombic interaction and form an exciton. This leads to thermalization loss in which excited electrons and holes try to come to the edge of the conduction and valence band, respectively.

3. *Charge separation and transportation*: the charge carrier's separation is the movement of electrons and holes toward their respective terminals under the influence of the field. It also depends on the mobility of charge carriers and the carrier lifetime.[28]

4. *Charge collection*: the photodetection efficiency also depends upon external factors such as electrodes. The quality of the electrode will determine how much charge is collected from the active material.[29]

There are different losses associated with the photodetector at each stage starting from the incident photon until the flow of the output current as shown in Fig. 2. These losses are the combination of multiple issues, such as reflection or scattering of incident photons, recombination loss, transportation loss, and contact losses. For an n-type Si-based screen printed solar cell utilizing a polysilicon passivating contact, the resistive and recombination losses contribute to 63%.[30] A bare Si solar cell causes about 30% of reflection losses.[31] An ideal photodetector should have zero losses, and a practical photodetector varies from the ideal photodetector because of the above-mentioned losses only. The quality of a photodetector is dependent upon how much it is inclined towards the ideal photodetector as determined by the following figures of merit:

• *Sensitivity*: it represents the change in the output current when light is incident with respect to the current under dark conditions. It is the ratio of the photogenerated current (I_{ph}) to the thermally generated current under dark conditions (I_{dark}).[32]

$$\text{Sensitivity} = \frac{I_{ph}}{I_{dark}} \quad (6)$$

High sensitivity is an essential requirement for any photodetection application such as medical diagnosis, optical communication, and many others.

• *Rise time and fall time (s)*: rise time and fall time define the rate at which the photodetector generates output with respect to the change in input conditions (illumination). In general, the rise time is the time taken for the output to change from 10% to 90% of the final value while the fall time is the time taken for the output to change from 90% to 10% of the initial value.[33] The rise time and fall time are of great importance in various applications such as optical communication, optical storage, LiDAR, time-resolved spectroscopy, and terahertz imaging. Detectors with a superior rise time are gen-

erally treated as ultrafast photodetectors, thus rise time represents the speed of the photodetector.

• *Responsivity (A W^{-1})*: the response of the device in terms of output current to input photon flux (optical power intensity) gives the responsivity.[32] This figure of merit directly correlates the system's input with the system's output and thus can be seen as the transfer function of the photodetector. A prerequisite for applications like fibre-optic communication, astronomical observation, and medical diagnosis is the high responsivity of the photodetectors.

$$S(\lambda) = \frac{J_{ph}(\lambda) - J_{dark}}{P_{opt}(\lambda)} \quad (7)$$

where $S(\lambda)$ is the responsivity, J_{ph} is the photocurrent density, J_{dark} is the dark current density, and P_{opt} is the optical power density at any wavelength (λ).

• *External quantum efficiency (%)*: the chain effect that leads to the sensing mechanism of photodetectors starts with decreasing the phonon flux. The generated electron–hole (e–h) pair with respect to incident photon flux density gives the photodetector's internal quantum efficiency (IQE). The generated e–h pairs are expected to be extracted *via* an external circuit leading to current flow in the circuit, but this process also loses charge pairs due to recombination and trap states. This loss is accommodated with an external quantum efficiency (EQE) which gives the ratio of the number of e–h pairs collected at the terminals with respect to the number of incident photons.[34] The maximum EQE one can achieve is equal to the IQE, thus representing the device's photogeneration, extraction, and collection efficiency. High efficiency is desired for every application where a photodetector is required.

$$EQE(\lambda) = \frac{\frac{J_{ph}(\lambda) - J_{dark}(\lambda)}{q}}{\frac{P_{opt}(\lambda)}{h\nu}} \quad (8)$$

Finally using eqn (7) with eqn (8), we can write:

$$EQE(\lambda) = 1240 \times \frac{S(\lambda)}{\lambda} \quad (9)$$

The EQE of a detector depends on the photon flux (ϕ) and the reflectivity (R).[35] Assuming the detector thickness is d as shown in Fig. 3(a), then $\phi(1-R)$ amount of flux will enter the detector material. The $\phi(1-R)$ amount of flux, will go through the absorption in the detector's material depending upon the absorption coefficient (α) as shown in Fig. 3(b) and (c).

$$\text{Absorbed energy} = \phi(1-R)(1-e^{-\alpha d}) \quad (10)$$

where $\phi(1-R)e^{-\alpha d}$ indicates the transmitted flux from the detector material. Not all photons absorbed may contribute to the photocurrent, some may result in phonons. Similarly, some of the generated e–h pairs will be lost due to recombination. Therefore, the generated e–h pairs that contribute to photocurrent (n) can be written as:

$$n = \phi(1-R)(1-e^{-\alpha d})\zeta \quad (11)$$

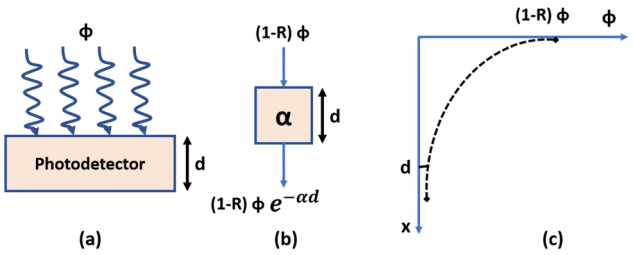

Fig. 3 (a) Schematic of a photodetector showing incident flux (ϕ), (b) illustration of incident intensity with respect to an absorption coefficient (α), and (c) illustration of variation due to absorbed energy in a photodetector.

where ζ is the defect parameter and depends on the defects in the detector material ($0 < \zeta < 1$). Then the EQE can be written as the ratio of generated e–h pairs to the incident photon flux

$$\eta = \frac{n}{\phi} = (1-R)(1-e^{-\alpha d})\zeta \quad (12)$$

The EQE of the detector can be maximized by tuning R, αd, and ζ as discussed below:

- The reflection can be minimized by utilizing an anti-reflection coating (ARC). The ARC is made for a particular wavelength only.

- By making αd large. This will decrease the $e^{-\alpha d}$ term and thus increase the EQE.

- ζ can be minimized by meticulous fabrication of the detector material. Improvement in ζ can be observed by minimizing defects and also utilizing charge transport layers for faster extraction.[36,37]

• *Detectivity (Jones or cm Hz$^{1/2}$ W^{-1})*: the detectivity of a photodetector is the minimum number of photons (photon flux density) required to generate the current in the external circuit.[38] The output current is impacted by the device's internal current (thermal current). The detectivity of a photodetector is inversely proportional to the noise-equivalent power (NEP). Thus, the detectivity decreases with an increase in noise current. Applications like medical diagnosis and astronomical observations require very high detectivity.

$$D^*(\lambda) = \frac{S(\lambda)\sqrt{A\Delta f}}{\sqrt{\langle i_n^2 \rangle}} \quad (13)$$

where A is the contact electrode area, Δf is the bandwidth, and $\langle i_n^2 \rangle$ is the noise-equivalent power.

• *Spectral selectivity*: the importance of a photodetector is observed from its discriminating behaviour between photons of different energies. This behaviour is generally classified using spectral selectivity, which depends upon the effective response width given as the FWHM.[12] This criterion is important for all applications that require precise detection of the photon energy.

The losses associated with a photodetector are undesirable and limit the performance of a photodetector. By utilizing suitable device engineering techniques, these losses can

be minimized to a certain extent and hence there will be obvious improvement in the figures of merit. In other words, device engineering in self-powered photodetectors revolves around optimizing the performance parameters. This includes enhancing light absorption, charge carrier generation, and extraction, and minimizing losses due to recombination and resistance. So, engineers can work on the materials, interfaces, and device architectures to achieve these goals.

3 Material specifications

The specifications of materials for self-powered photodetectors depend on the application and desired performance characteristics. However, the general considerations for materials are as follows:

- *Bandgap*: the bandgap of the material should match the wavelength of the light and should be less than or equal to the energy of the photon for e–h pair generation. For example, the energy brought by the red light (720 nm) photon is 1.72 eV while the energy brought by the violet light (400 nm) photon is 3.1 eV.
- *Mobility*: the mobility of the charge carriers in the semiconductor material should be very high. It has an impact on the speed and ability to detect weak signals. However, a higher mobility results in a higher dark current, but the dark current can be minimized by utilizing junction engineering.[39]
- *Stability*: under various operating conditions such as moisture, heat, and exposure to light, the semiconductor's electrical and optical properties should remain stable.
- *Cost*: the cost of the material should be as low as possible. It is a very important parameter for large-scale applications.

The different materials utilized nowadays for self-powered photodetectors are:

Wide bandgap semiconductors:[40,41] these materials have large bandgaps and are suitable for ultraviolet and visible light detection. Some of the examples are ZnO, GaN, InP, and SiC.

0D, 1D, and 2D materials:[42,43] these materials have a high surface-to-volume ratio, which can make them more sensitive to light than traditional bulk semiconductors.[44]

As research into self-powered photodetectors continues, new materials and device architectures are being explored. This is leading to the development of more efficient, sensitive, and versatile self-powered photodetectors for a variety of applications.

4 Origin of the electrical field

For photodetectors to function appropriately, it is necessary to carry out two essential processes: the separation and collection of photogenerated charge carriers through electrodes. The effectiveness of charge carrier separation depends on the electric field that is established across the depletion region. On the other hand, several factors, including but not limited to an electric field, carrier transit time, trap states, and carrier mobility, influence the collection ratio.[46] It is worth noting that the electric field, which can be either internal or externally enhanced, is the driving force for separating and collecting charge carriers. External sources, such as batteries, are typically used to provide the electric field in conventional photodiodes. Recent research has focused on replacing external battery sources with photovoltaic units and piezo-nanogenerators to develop self-powered photodetector assemblies as a potential replacement for traditional photodetectors.[16,47–49] Xu *et al.*[47] successfully demonstrated that the lateral integration of 700 rows of ZnO nanowires (NWs) could generate 1.26 V when subjected to a strain of 0.19%. This system was utilized to power the UV sensing capabilities of ZnO NWs. Bie *et al.*[45] fabricated a self-powered photodetector that incorporated an energy harvesting unit. This device features a CdSe NW that is powered by an n-ZnO/p-GaN photovoltaic unit, as illustrated in Fig. 4. The device demonstrates exceptional transient response, with a rise time of 20 μs and a fall time of 219 μs. Additionally, it functions as an optical AND gate for both red and UV light. In their work, Wu *et al.*[48] employed a flexible piezo-nanogenerator as the power-generating unit. They developed a self-powered photodetector utilizing a PZT NW textile nanogenerator, with the UV sensing element comprising ZnO NWs. The nanogenerator is capable of producing a maximum output voltage of 240 mV and a current of 2.5 nA. The voltage drop across the UV sensing unit can be utilized to estimate the level of light intensity. As the UV intensity increases, the generation of charge carriers also increases, leading to a reduction in resistance and a voltage drop across the UV sensing unit. Apart from the photovoltaic unit and piezo-nanogenerator, micro-supercapacitors have also been utilized as an energy harvesting unit by researchers. A flexible photodetector with micro-supercapacitors integrated on a chip was developed by Xu *et al.*[49] The photodetector comprises CdS NWs, while the micro-supercapacitor is made from reduced graphene oxide (rGO).

Lu *et al.*[16] developed a nanosystem consisting of a photodetector and a solar cell-based energy harvesting unit. The system utilized a perovskite-based ($CH_3NH_3PbI_3$) solar cell to power the perovskite-based photodetector, as illustrated in Fig. 5. The integration-based systems, where external energy

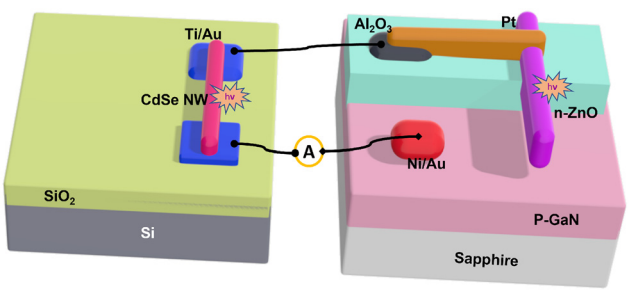

Fig. 4 Schematic of a CdSe NW-based photodetector utilizing a ZnO/GaN-based energy harvesting unit.[45]

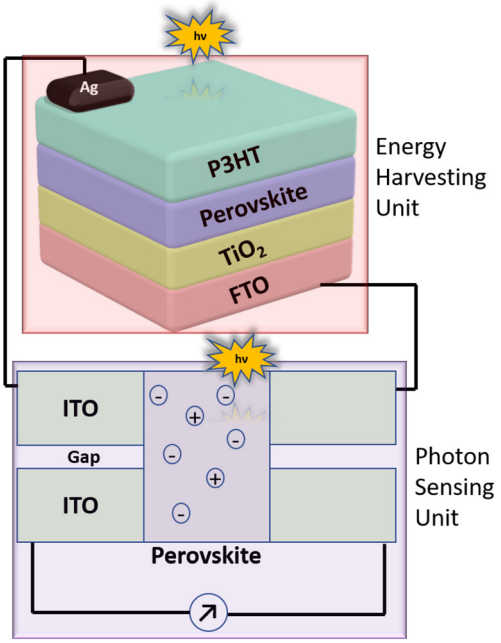

Fig. 5 Schematic of a photodetector-solar cell-based nanosystem.[16]

harvesting units are coupled with photodetectors, can provide excellent electrical and optical properties, but they lack the flexibility to be easily integrated into an integrated circuit due to their increased size or complex design. Thus, interest in compact systems that rely on utilizing the internal field for charge carrier extraction is increasing and these systems show potential for application in the development of next-generation nanoscale integrated self-powered photodetectors.

The following study delves into the topic of self-powered photodetectors, which are capable of generating power independently without the need for any external energy harvesting unit. The performance of these devices depends on several factors, including the materials utilized, the type of junction formed, the type of electrode used, and the incorporation of various effects. Each of these performance enhancement factors is discussed in detail in the following sections.

5 Utilization of ETLs and HTLs

The photogenerated carriers must be separated and collected before they recombine for the proper functioning of a photodetector.[50] However, materials with a low carrier lifetime suffer from the issue of early charge carrier recombination, which necessitates device engineering techniques to collect the photogenerated charge carriers effectively. Utilizing the electron-transport-layer (ETL) and hole-transport-layer (HTL) can significantly improve the collection of photogenerated carriers in low-carrier lifetime materials. The ETL and HTL refer to the highly doped n-type and p-type semiconductor layers respectively. They are crucial in creating an electric field that drives the charge carriers toward the respective terminals, thus preventing recombination. The formation of the depletion region enables the ETL to attract electrons, while the HTL attracts holes and repels charges of opposite polarity.

Fig. 6(a) depicts a photodetector that employs an ETL and an HTL. Light enters from the FTO/ITO side, which serves as a transparent conductor, resulting in 100% illumination area. The band diagram is shown in Fig. 6(b), illustrating that the ETL and HTL assist in moving electrons and holes toward the cathode and anode, respectively. As a result, the probability of charge carrier recombination is reduced. Improved carrier extraction results in enhanced figures of merit of the self-powered photodetector, such as response time, sensitivity, detectivity, responsivity, and EQE. Xie *et al.*[51] fabricated a blue light hybrid self-powered photodetector. The device employs a hybrid heterojunction between an n-TiO_2 nanorod array (NRA), an inorganic material, and a p-spiro-MeOTAD, an organic material, where TiO_2 act as an ETL and spiro-MeOTAD act as the active layer and HTL. The photodetector exhibits a rapid response with a rise time of 120 ms and a fall time of 60 ms. Kumar *et al.*[52] also developed a self-powered photodetector with an ETL-only architecture. This photodetector is believed to be the first to be based on quantum dots (QDs). The device forms a Schottky junction between Au electrodes and CdSe QDs, with CdSe being the active layer. The ETL, consisting of ZnO QDs, enables efficient electron extraction. The device exhibited an excellent transient response, with a rise-time of 17.9 ms and a fall-time of 18 ms. Goel and Kumar[53] improved upon the device built by Kumar *et al.*[52] by introducing an HTL layer made of MoO_x and incorporating a transparent ITO electrode. They utilized MoO_x along with ZnO QDs and CdSe QDs in the device. They observed a 15% improvement in key performance metrics such as rise time, responsivity, detectivity, and EQE compared to the device without the HTL. Shen *et al.*[54] achieved an even better transient response by incorporating TiO_2 and spiro-MeOTAD layers as the ETL and HTL, respectively, in their self-powered photodetector. The device was fabricated on a flexible ITO/PET substrate and the perovskite QDs ($CsPbBr_3$) were utilized as the active layer. The resulting device exhibited an extremely fast transient response, with

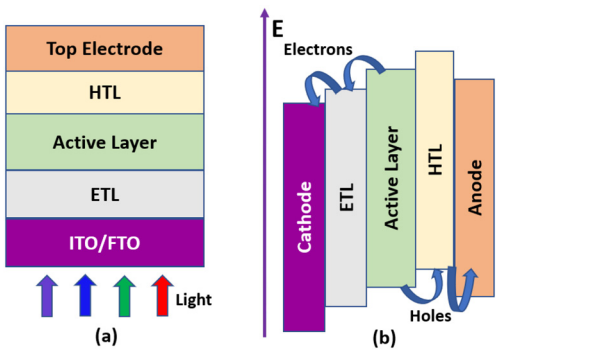

Fig. 6 (a) Schematic of a photodetector with back illumination utilizing an ETL and an HTL, (b) energy band diagram of the photodetector.

a rise time of only 2.3 ms. Zhou *et al.*[55] demonstrated that the doping of charge transport layers could also enhance the performance of self-powered photodetectors. They[55] fabricated a visible self-powered photodetector using Ga-doped ZnO nanorods (NRs) and the $MAPBI_3$ perovskite as an active layer. The Ga-doped ZnO NRs were utilized as the ETL, and the device exhibited an ultrafast transient response with a rise/fall time of 2 ms.

According to Li *et al.*,[56] various materials can be used as the HTL and ETL in self-powered photodetectors, including TFB, TIPS pentacene, PEDOT:PSS, NiO_x, MoO_x, V_2O_5, CuSCN, BCP, Bphen, C_{60}, PEIE, PFN, PEI, ZnO, TiO_2, SnO_2, Cs_2CO_3, and others. An HTL layer is crucial for the organic material-based active layer, as without it, there would be little to no response. TiO_2 and ZnO are commonly used ETLs due to their excellent hole-blocking property and transparency to solar radiation. Voroshazi *et al.*[57] conducted a stability analysis of various ETLs and HTLs, finding that ZnO and TiO_2 have better stability than other organic ETLs. Regarding HTLs, they compared the performance of MoO_3 and PEDOT:PSS, and surprisingly, found that PEDOT:PSS-based devices had higher stability than MoO_3-based devices. The MoO_3-based device showed a stability of approximately 4000 h, while the PEDOT:PSS-based device showed a stability of approximately 5000 h. Similarly, Jarwal *et al.*[36] investigated the impact of seven different organic HTLs on the performance of the perovskite-based solar cells. After conducting an extensive study, they discovered that using spiro-OMeTAD as an HTL led to better performance metrics than the other six organic HTLs, which were PTAA, PQT, P3HT, MEH-PPV, nPB, and PEDOT:PSS.

This section states that the device engineer should select the ETL and HTL wisely before fabricating the self-powered photodetector since the ETL and HTL are essential for organic materials since organic materials suffer from lower mobility and the utilization of the ETL and HTL facilitates the movement of charge carriers towards their respective terminals, resulting in improved figures of merit.

6 Bandgap engineering

Bandgap engineering involves adjusting the bandgap of a material to optimize its electronic and optical characteristics for a specific purpose. In the context of a photodetector, bandgap engineering can enhance its performance and spectral coverage. By doing so, light absorption can be improved, leading to better figures of merit. In general, the bandgap is modified using the following techniques:

6.1 Quantum confinement

The process involves constructing a structure with dimensions comparable to the Bohr radius or the electron's wavelength, such as a quantum dot, nanowire, or nanosheet, which results in modifications to the material's electronic properties as a function of particle size. The specific form of quantum confinement gives rise to various material types, as described below[44,58] and shown in Fig. 7.

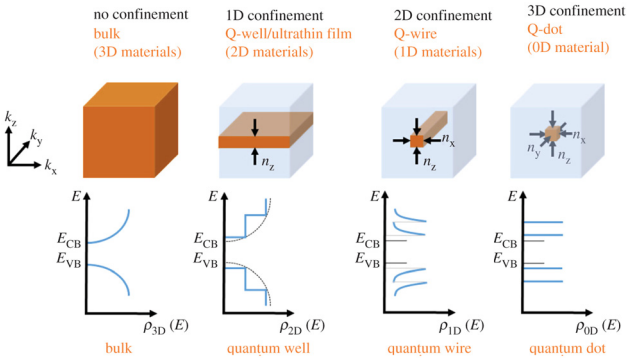

Fig. 7 Types of materials based on confinement.[58] Published with "Royal Society Open Science" as open access, 2018.

- *3-D materials (no confinement)*: electrons can move in all three dimensions, also known as bulk materials.
- *2-D materials (1-D confinement)*: 2-D materials refer to materials that permit unrestricted electron motion in two dimensions while restricting it in one dimension, commonly referred to as quantum sheets or quantum wells.
- *1-D materials (2-D confinement)*: in 1-D materials, electrons can move freely along one direction while their motion is restricted in the other two dimensions, commonly called nanowires.
- *0-D materials (3-D confinement)*: in 0-D materials, such as quantum dots (QDs), the motion of electrons is restricted in all three dimensions. The constrained structure of QDs results in unique charge transport behaviour compared to other dimensional materials (1-D, 2-D, and 3-D). In QDs, the primary charge transport mechanism is through the tunneling and hopping of charge carriers.[60]

Due to quantum confinement, the bandgap of a material increases as the particle size decreases. CdSe nanoparticles of varying sizes were synthesized by Murray *et al.*,[61] and they found that the bandgap decreased (from 2.4 to 1.7 eV) with an increase in particle size (from 2 to 20 nm). Kumar *et al.*[59] also demonstrated the effect of quantum dot size on the photodetector response by using a heating technique to change the size of ZnO QDs during annealing. As shown in Fig. 8, they obtained bandgaps of 3.42, 3.26, and 3.23 eV for sizes of 4.42, 8.74, and 13.89 nm, respectively. The relationship between the bandgap of a QD as a function of its particle size (radius of QD, R) and its bulk counterpart can be described by the following equation, according to Murphy *et al.*:[62]

$$E_g(\mathrm{QD}) = E_g(\mathrm{bulk}) + \left(\frac{h^2}{8R^2}\right)\left(\frac{1}{m_e} + \frac{1}{m_h}\right) - \frac{1.8e^2}{4\pi\varepsilon_0\varepsilon R} \qquad (14)$$

where E_g(QD) is the bandgap of the QDs, E_g(bulk) is the bandgap of the bulk semiconductor, e is the electronic charge, m_e is the effective mass of the electron, m_h is the effective mass of the hole, ε is the dielectric constant of the semi-

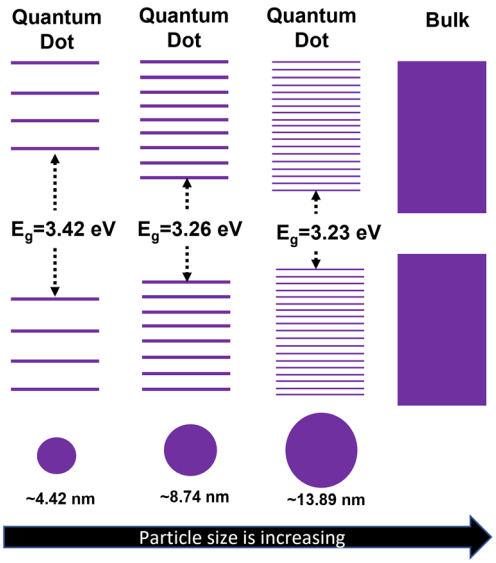

Fig. 8 Demonstration of variation of the bandgap of quantum dots (QDs) with respect to the size of the QDs.[59]

conductor and ε_0 is the permittivity of free space or vacuum. Also, the carrier mobility in hopping-dominated systems like QDs can be written as:[60]

$$\mu(E) = \frac{R(E)}{E} \times d \tag{15}$$

The carrier mobility in the equation is denoted as $\mu(E)$ and the electric field-dependent hopping rate as $R(E)$, while d represents the distance to the nearest hopping neighbour. Gilmore *et al.*[63] modeled the hopping rate as a function of the relative positions and energetics of nearby QDs as indicated in eqn (16). They utilized the Miller–Abrahams rate equation to describe the hopping rate of an electron from the ith QD to the jth QD in the conduction band.

$$k_{i\to j} = \begin{cases} k_0 \exp(-\beta r_{ij}) \exp\left(-\dfrac{(\varepsilon_j - \varepsilon_i)/2}{k_B T}\right) & \varepsilon_j > \varepsilon_i \\ k_0 \exp(-\beta r_{ij}) & \text{otherwise} \end{cases} \tag{16}$$

where ε_i and ε_j are the bandgap energies of the ith QD and the jth QD respectively. The parameters r_{ij}, k_0, and β are the edge-to-edge distance between the QDs, the intrinsic hopping rate, and the tunneling parameter measured in nm^{-1}, respectively. As the size of the QDs decreases, the number of hopping sites increases, resulting in a decrease in effective mobility. This characteristic limits the use of QDs in high-mobility devices but can be advantageous for photodetectors, where the dark or noise current must be negligible.

6.2 Doping and alloying

Alloying and doping are two common techniques for modifying material properties. Alloying involves mixing two or more elements to form a new material with different properties, while doping introduces impurities into a material to modify its electrical and optical properties. The main difference is that alloying changes the material's crystal structure,[69] whereas doping does not alter the crystal structure but changes its electrical and optical properties.[70] Boruah *et al.*[64] investigated the effect of doping on photocurrent in a ZnO NRA. The nanorods were doped with F, Cl, Br, and I, and the device was based on an ITO/doped:ZnO NR/PEDOT:PSS/Ag UV photodetector. The Cl-doped ZnO-based device exhibited enhanced figures of merit with a sheet charge density of 7×10^{10} cm^{-2} and a photocurrent of 220 nA. The sheet charge densities and corresponding photocurrents for doped ZnO nanorods are listed in Table 1. The results of photoluminescence analysis demonstrate a blueshift in the bandgap of ZnO NRs due to doping. Abbasi *et al.*[65] investigated the impact of varying levels of Cd doping in ZnO NRs, ranging from 0% to 7%. They calculated various parameters to study the optical behaviour of the devices, as listed in Table 2. The highest sensitivity, responsivity, and detectivity were obtained with 7% Cd doping, while the fastest response was achieved with 5% Cd doping. The bandgap remained consistent with doping, but the photoluminescence intensity increased, indicating a higher number of direct generation and recombination events suitable for photodetection applications. Kumar *et al.*[66] also examined the effect of Al and Mg doping of CdS and deter-

Table 1 Photocurrent of a photodetector at different sheet charge densities under a fixed UV illumination intensity of 3 mW cm^{-2} (ref. 64)

S. no	Photodetector	Sheet charge density (cm^{-2})	Photocurrent (nA)
1	ZnO NRs	0.323×10^{10}	40
2	F:ZnO NRs	4.62×10^{10}	150
3	Cl:ZnO NRs	7×10^{10}	220
4	Br:ZnO NRs	3.8×10^{10}	140
5	I:ZnO NRs	0.92×10^{10}	90

Table 2 Different parameters of a ZnO NR based photodetector with varying percentages of Cd[65]

Sample (Cd%)	Avg. diameter (nm)	Avg. length (nm)	Photocurrent (nA)	Rise time (s)	Decay time (s)	Sensitivity (I_{ph}/I_d)	Responsivity (μA W^{-1})	Detectivity (Jones)
0%	50–60	300–400	32.08	18	13	110.62	2.07	0.22×10^9
3%	50–70	500–650	162.15	8	10	463.28	10.46	0.98×10^9
5%	40–60	600–700	320.21	2.5	4	762.40	20.66	1.8×10^9
7%	60–75	850–1000	460.10	5	6	920.30	29.68	2.4×10^9

Table 3 Observed parameters of CdS thin film photodetectors[66]

Thin film materials	Rise time (ms)	Decay time (ms)	EQE (%)	Responsivity (A W^{-1})	Detectivity (Jones)
CdS	840	910	41.36	0.17	7.12×10^{10}
CdS:Mg (3%)	780	880	327.46	1.40	4.05×10^{11}
CdS:Al (3%)	750	850	497.29	2.13	5.23×10^{11}
CdS:Mg (3%) & Al (3%)	820	890	72.50	0.31	1.43×10^{11}

mined the resulting devices' optical parameters, such as responsivity, detectivity, and EQE. They discovered that the material's bandgap varied depending on the dopant, ranging from 2.3 eV to 2.25 eV. The extracted device parameters are presented in Table 3. The study concludes that doping with various materials can shift the bandgap, while varying the doping concentration can directly influence the charge generation and recombination mechanisms.

Researchers have also tried to modify the bandgaps of the materials by alloying as the alloyed material has more tolerance to lattice mismatch and can be utilized to tailor the electronic and optical properties of the photonic devices.[71] Hao *et al.*[71] employed alloy engineering to tailor the bandgap and observed a decrease in the bandgap of $InSe_{1-x}Te_x$ with an increase in 'x' values. Conversely, the bandgap of $InSe_{1-x}S_x$ increased with increasing 'x'. For a constant value of x = 0.2, the bandgap of $InSe_{0.8}Te_{0.2}$ is found to be 1.11 eV, while that of $InSe_{0.8}S_{0.2}$ is 1.34 eV. In a similar approach, VK and Rao also investigated the effect of varying the value of 'x' on the bandgap of $Cd_xZn_{1-x}S$. The value of 'x' was determined using EDAX analysis, and the bandgap was obtained using the Tauc relation (eqn (17)) from UV-Vis spectrophotometry. Their findings indicate that the material's bandgap decreases as 'x' increases.

$$\alpha h\nu = A(h\nu - E_g)^n \quad (17)$$

where n = 0.5 for an allowed direct transition, ν is the frequency, h is Planck's constant, E_g is the bandgap of the film, and A is a constant. Alonso-Álvarez *et al.*[67] presented the impact of varying alloy compositions of Al, In, As, Ga, P, and Sb on the lattice constant and bandgap in comparison with Si and Ge. The findings are depicted in Fig. 9. The alloying process is commonly employed in photodetectors to attain tunability and selectivity in the spectrum. Yu *et al.*[72] investigated the electrical properties of $InSe_{1-x}Te_x$ alloy used to fabricate a tunable self-powered photodetector. This device shows broadband photodetection with 400 nm to 1000 nm spectral coverage. The peak responsivity is 14.1 mA W^{-1} at 900 nm under self-bias conditions for x = 0.18. Joseph *et al.*[68] also investigated the impact of alloying ZnO with various metals, resulting in $Zn_{0.95}M_{0.5}O$ where 'M' = Cr, Mn, Fe, Co, and Ni in the structure. The study revealed that alloying changed the bandgap, leading to different metal doping effects, *i.e.*, blue shifting (Mn, Co) and red shifting (Cr, Fe, Ni), also illustrated in Fig. 10. Ebrahimi and Yarmand[73] fabricated $Sn_xZn_{1-x}S$ com-

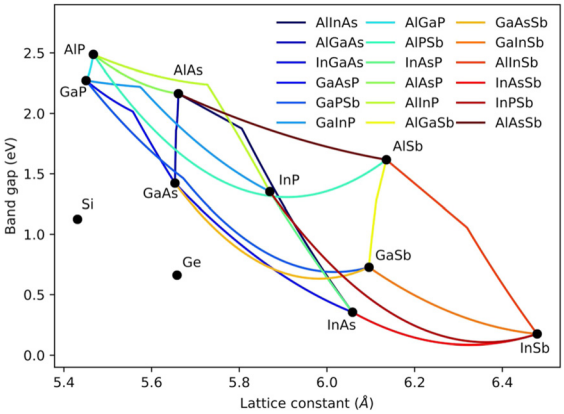

Fig. 9 Variation of bandgap with lattice constant in different alloyed materials,[67] Published by "Springer Nature" as open access, 2018.

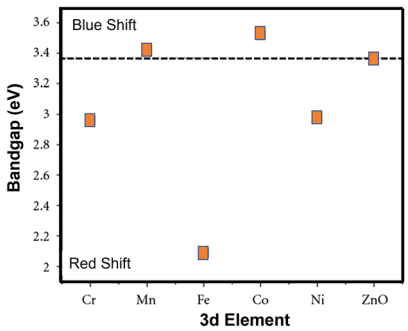

Fig. 10 Variation in bandgap with respect to dopants for the host ZnO.[68]

posite material where x varied from 0 to 1 with an Au-based Schottky contact. The solvothermal process is used for the preparation of the active layer. They observed a bandgap tuning effect; with an increment in the Sn concentration, the bandgap decreases, as shown in Table 4. The resulting device showed spectrum selectivity, with a peak around 400 nm and an FWHM of less than 100 nm.

6.3 Superlattice

A superlattice is a structure that involves the layering of multiple materials with different bandgaps, resulting in a combined bandgap determined by the thickness and bandgap of each material.[75] Researchers have utilized superlattice struc-

Table 4 Bandgap of $Sn_xZn_{1-x}S$ thin films for different values of x [73]

S. no	Sample	Bandgap (eV)
1	Pure ZnS	4.2
2	$Sn_{0.02}Zn_{0.98}S$	4.14
3	$Sn_{0.04}Zn_{0.96}S$	4.10
4	$Sn_{0.06}Zn_{0.94}S$	3.99
5	$Sn_{0.08}Zn_{0.92}S$	3.91
6	$Sn_{0.1}Zn_{0.9}S$	3.87
7	$Sn_{0.12}Zn_{0.88}S$	3.83

tures in the development of various photodetectors. For instance, Li *et al.*[76] developed a transparent UV photodetector using an InGaZnO-based superlattice structure with a responsivity of 64 600 A W^{-1} at −20 V. Similarly, Delli *et al.*[74] fabricated a mid-infrared InAs/InAsSb superlattice photodetector as shown in Fig. 11 with an EQE of 25.6% at 200 K and a maximum specific detectivity of 3.65×10^{10} Jones with top illumination at 100 mV, although no significant work has been reported for self-powered photodetectors utilizing a superlattice structure.

In summary, the bandgap is a critical parameter for determining the absorption characteristics and current output of a self-powered photodetector. Engineers carefully select semiconductor materials with appropriate bandgaps to achieve optimal energy conversion efficiency in photodetector designs.

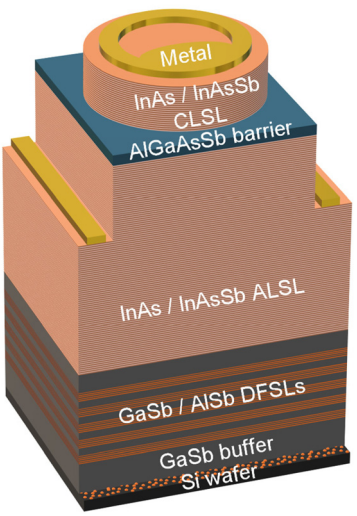

Fig. 11 Schematic of the InAs/InAsSb type-II superlattice structure grown on GaSb/AlSb/Si buffer, using AlSb/GaSb dislocation filters.[74] Published with "American Chemical Society" as open access, 2019.

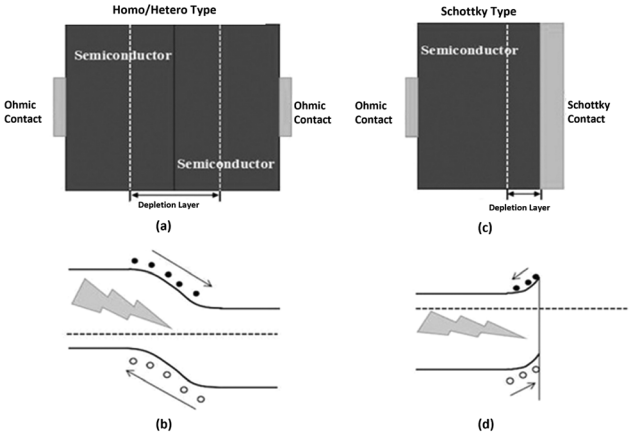

Fig. 12 (a) Schematic and (b) band diagram of homo/heterojunction-based self-powered photodetectors. (c) Schematic and (d) band diagram of Schottky junction-based self-powered photodetectors.

7 Junction engineering

In self-powered photodetectors, the photogenerated charge carriers should be separated and collected at the respective electrodes before they recombine. This separation and collection are governed by the built-in electric field.[17,77] The built-in field is provided by the different junctions formed like homojunctions, heterojunctions, and Schottky junctions. The operational mechanisms of various self-powered photodetectors are demonstrated in Fig. 12. The photogenerated charge carriers are separated by an electric field set up by the immobile ions or fixed charges in the depletion region.

7.1 Junction between semiconductors (homo/heterojunction)

The homojunction is the most commonly used type of junction, which utilizes the same kind of semiconductors. Shen *et al.*[78] fabricated a device using the n-ZnO/p-ZnO:(Li,N) homojunction. The fabricated detector shows an FWHM of 9 nm due to the filtering action of undepleted p-ZnO (doped). They[78] showed that increasing the bias voltage led to an increment in the depletion region and a reduction in the FWHM. Another frequently employed technique to create efficient self-powered photodetectors is using heterojunctions, which involve materials with varying bandgaps.[79] This process involves the epitaxial growth of different layers, making heterojunctions easy to fabricate. Depending on the types of semiconductors forming the junction, heterojunctions can be classified into two categories. Isotype heterojunctions are formed when the junction is between semiconductors of the same type (p–p or n–n). In contrast, anisotype heterojunctions are formed when the junction is between semiconductors of different types (p–n). Hassan *et al.*[80] fabricated a self-powered photodetector using p-Si and n-ZnO NRs (anisotype heterojunction). This device demonstrated a response time of 25 ms and a recovery time of 22 ms, with a sensitivity of approximately 8000% under UV illumination.

Hybrid heterojunctions, which combine the benefits of both organic and inorganic semiconductors, have been explored by researchers. This type of junction offers the low-cost and environmentally friendly advantages of organic semiconductors and the high carrier mobility of inorganic semiconductors.[81] For instance, Kumar *et al.*[82] developed a self-powered photodetector using CdSe QDs and PQT-12 hybrid heterojunctions. The device has a spectral peak at approximately 420 nm and a rise and fall time of 15.32 and 12.01 ms, respectively. Li *et al.*[83] developed a self-powered photodetector based on CdSe and p-Sb_2 $(S_{1-x}Se_x)_3$, as illustrated in Fig. 13(a). The photogenerated electrons move toward FTO while holes move toward spiro-OMeTAD, as shown in Fig. 13(b). The device covers a spectral range from 650 nm to 900 nm. By varying the CdSe thicknesses and Se concentration, the researchers achieved selectivity, as shown in Fig. 13(c) and (d), respectively.

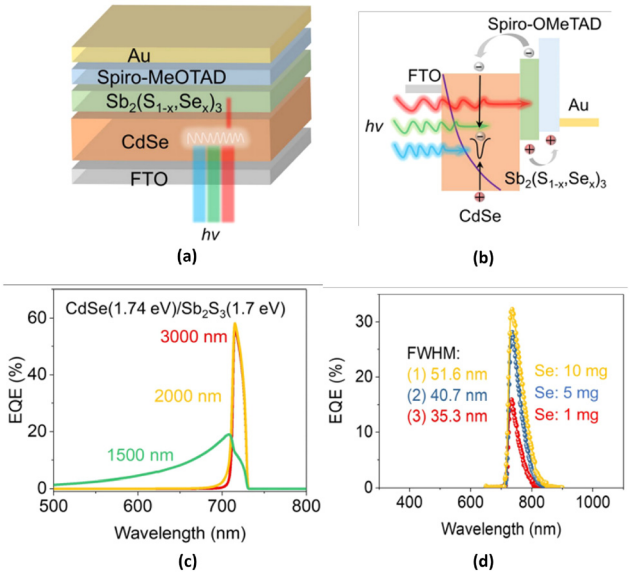

Fig. 13 (a) Schematic of the self-powered photodetector, (b) schematic of carrier transport in the device, (c) EQE for different CdSe thicknesses, and (d) EQE for different Se concentrations.[83] Published by "Wiley-VCH" as open access, 2021.

7.2 Junction between a metal and a semiconductor (Schottky junction)

The interface between a metal and semiconductor can exhibit three distinct behaviours: ohmic, tunneling, and Schottky junctions.[50] In the case of ohmic and tunneling contacts, charge carriers can flow freely without encountering any barriers, and thus these contacts serve purely as a means of connection. On the other hand, Schottky junctions provide a rectifying barrier that responds to bias and features a depletion region that extends primarily toward the semiconductor. It is important to consider the metal and semiconductor's work function to ensure the formation of an efficient Schottky junction. When forming a junction between an n-type semiconductor and metal, the metal's work function should be greater than the semiconductor's. Conversely, for a p-type semiconductor and a metal junction, the semiconductor's work function should be greater than the metal's. Nonetheless, it is worth noting that the minimum criteria for forming a Schottky junction involve the metal's work function and the semiconductor's electron affinity.[50] Devices based on Schottky junctions are known to be more sensitive and faster than those based on two-ohmic contacts. The metal used for Schottky contacts can include graphene, Au, Ag, and others. Graphene, being a 2D material with high mobility, is a promising candidate for self-powered photodetectors. Jin *et al.*[109] utilized graphene in a Schottky contact with a CdSe nanobelt to create a self-powered photodetector with high photosensitivity. The fabricated device shows a photosensitivity of ~3.5 × 10^5 and a fast transient response time, with a rise and fall time of 82 and 179 μs, respectively. A Schottky junction between graphene and a CdSe nanobelt was also fabricated by Gao *et al.*[110] This structure was implemented on a flexible substrate, and the researchers achieved better transient times with a rise and fall time of 70 and 137 μs, respectively. However, the study did not investigate whether the photodetector's response was affected by the rolling or bending of the flexible substrate. Duan *et al.*[85] developed a self-powered photodetector using a graphene-based Schottky contact in conjunction with a ZnO:Al NRA and found an improved rise time and responsivity of 37 μs and 39 mA W^{-1}, respectively. Benyahia *et al.*[89] developed a self-powered photodetector utilizing Au as a Schottky contact with a ZnO–ZnS active layer prepared at 500 °C. The detector exhibits a response across a broad spectral range of 300 to 900 nm but cannot efficiently discriminate photons, a crucial property of photodetectors. Purusothaman *et al.*[90] developed a self-powered photodetector utilizing a floral-like ZnO NR structure with an Ag-based Schottky contact. The device was fabricated on a flexible PVDF substrate, demonstrating a responsivity of 22.76 mA W^{-1}. In the field of research, Schottky junction-based devices are often preferred over homojunction and heterojunction-based devices due to their faster transient times and ease of fabrication.[111] A list of different self-powered photodetectors categorized based on junction engineering can be found in Table 5.

In summary, junction engineering in self-powered photodetectors focuses on creating favourable conditions for efficient charge separation, minimizing recombination losses, and optimizing band alignment, facilitating effective charge transfer between different semiconductor layers. These efforts contribute to improving the overall performance and efficiency of self-powered photodetectors.

8 Surface passivation

At the surface of a semiconductor, atoms at the surface lack a bonding neighbour and this results in dangling bonds. These dangling bonds introduce a forbidden energy gap that charge carriers can use as recombination sites. Surface passivation is a technique used to improve the efficiency of detectors by creating a protective layer on their surface that reduces the number of defects and population of minority carriers. Thin films of a semiconductor material such as silicon nitride, SiN_x (for n-type surfaces), or aluminium oxide, AlO_x (for p-type surfaces), are grown on the detector's surface using chemical vapour deposition or atomic layer deposition techniques. These passivation layers reduce the recombination of electrons and holes, thereby improving the detector's overall response.[113]

Zeng *et al.*[112] fabricated a NIR self-powered photodetector using a graphene/Si nanotube array as shown in Fig. 14. In addition, surface passivation with methyl termination ($-CH_3$) is used to enhance the detector's figures of merit. With $-CH_3$ passivation, the device's sensitivity, responsivity, and detectivity are found to be 10^7, 0.328 A W^{-1}, and 6.03 × 10^{13} Jones, respectively, which are much higher than the figures of merit of the device without surface passivation.

In summary, surface passivation in self-powered photodetectors is essential for reducing surface recombination, improving carrier lifetimes, and enhancing the overall performance.

Table 5 Summary of different self-powered photodetectors in different junction categories

Structure materials	Structure category	Response (recovery) time	Responsivity (mA W^{-1})	Detectivity (Jones)	EQE (%)	Spectrum region	FWHM (nm)
Graphene/ZnO NW/graphene[84]	Schottky	—	~0.55	—	0.185	UV	~100
Graphene/ZnO:Al NRA-film[85]	Schottky	37 (330) μs	39	—	—	UV	<100
Graphene/H_2O_2-treated ZnO[86]	Schottky	32 ms	0.050	—	—	UV	—
Au-ZnO-Au MSM structure[87]	Schottky	—	20	—	—	UV	~100
Au/ZnO/GaN/Al_2O_3 [88]	Schottky anisotype heterojunction	731 (53.1) ms	95.8	2.9×10^{12}	—	UV	<100
Au-$Sn_xZn_{1-x}S$-Au MSM[73]	Schottky	—	47.1	1.64×10^{9}	—	UV	—
Au/ZnO–ZnS microstructured composite/Au MSM[89]	Schottky	22.5 (45.2) ms 22.3 (40.1) ms 25.2 (15.6) ms	3.34 1.05 0.47	8.9×10^{12} 2.8×10^{12} 1.4×10^{12}	—	UV–visible–NIR	>100
Floral-like F-ZnO NRs on PVDF[90]	Schottky	—	22.76	2.72×10^{10}	—	UV	—
Se/In–Ga microrod[91]	Schottky	124 (146) μs	408	1.30×10^{13}	—	UV-visible	>100
Au/CdSe QDs/ZnO QDs/n-Si[52]	Schottky isotype heterojunction	17.9 (18) ms	10.23	8.81×10^{9}	—	UV	>100
Pd(Au)/CdSe QDs/ZnO QDs/ITO[92]	Schottky isotype heterojunction	17.15 (28.9) ms	7.48 (2.7)	1.3×10^{10} (8×10^{9})	2.21% (0.87%)	—	~61 (190)
ZnO/GaN[45]	Anisotype heterojunction	20 (219) μ s	—	—	—	UV	<100
ZnO NRA/p-Si[80]	Anisotype heterojunction	25 (22) ms	—	—	—	UV	—
ZnO NR/p-CuSCN[93]	Anisotype heterojunction	0.5 (6.7) μ s	7.5	—	—	UV	<100
ZnO NR/p-CuSCN[94]	Anisotype heterojunction	~25 ns (4 ms)	50	—	—	UV	<100
ZnO NW array/graphene/CdS/electrolyte[95]	Heterojunction	5 ms	27.3, 4.3	—	—	UV, Visible	<100
ZIF-8@H:ZnO NRs/p-Si[96]	Anisotype heterojunction	252 (607) μ s	7070	2.14×10^{16}	—	UV-NIR	>100
ZnO–Co_3O_4 nanowire[97]	Anisotype heterojunction	6 s	21.80	4.12×10^{12}	—	Visible	—
CuI/In–Ga–Zn–O[40]	Anisotype heterojunction	2.5 (35) ms	0.6		—	UV	—
Carbon dot enhanced ZnO/graphite[98]	Heterojunction	2 (~3.2) s	9.57	4.27×10^{8}	—	UV	—
Cu_2ZnSnS_4 (CZTS) and MoS_2 [99]	Anisotype heterojunction	81 (79) ms	141	—	—	—	—
InGaZnO/p-silicon NW[100]	Anisotype heterojunction	~0.1 ms	530	—	—	UV	>100
p-NiO/n-Si[101]	Anisotype heterojunction	<85 ms	13.08, 46.02, 44.49	1.03×10^{11}, 3.65×10^{11}, 3.53×10^{11}	4.43, 8.62, 6.47	UV, red, NIR	—
CuI/$CsCu_2I_3$/GaN[102]	Anisotype heterojunction	8.8 (0.32) s	71.7	3.3×10^{12}	26.1	UV	<100
FTO/ZnO/perovskite + GaZnO NRs/MoO_3 [55]	Anisotype heterojunction	<2 ms	300	1.3×10^{12}	—	UV	>100
ZnO NWs/p-Si with Ga doping[103]	Anisotype heterojunction	1.4 (1.1) s	192	1.09×10^{13}	62.7	UV	<100
$SnS_2/ZnO_{1-x}S_x$ [104]	Anisotype heterojunction	49.51 (25.93) ms	8.28	5.09×10^{10}	—	UV to NIR	<100
N:ZnO-SpiroMeOTAD[105]	Hybrid anisotype heterojunction	200 (950) μ s	17	—	—	—	>100
ZnO@CdS core–shell nanorod arrays[106]	Anisotype heterojunction	20 ms	—	—	—	UV, visible	—
CdSe QD/PQT-12 [82]	Hybrid anisotype heterojunction	~12.01 (~15.32) ms	3.3	5.4×10^{9}	—	Visible	>100
p-ZnO:(Li,N)/n-ZnO[78]	Homojunction	—	~0.016	—	—	UV	9
Au-MgZnO-Au[107]	Schottky	0.23 (92) μs	2.22	4.4×10^{11}	—	UV	<100
n-NiO nanoflakes/AZO NRs[108]	Isotype heterojunction	~2 ms	85.12	1.74×10^{12}	—	UV	9
FTO/CdSe/$Sb_2(S_{1-x},Se_x)_3$/spiro-OMeTAD/Au[83]	Hybrid anisotype heterojunction	—	190	—	32.2	NIR	35.3
ITO/ZnO QDs/CdSe QDs/MoO_x/Pd[53]	Schottky aniso + iso type heterojunction	13.56 (26.56) ms	11.8	1.74×10^{10}	3.73	Violet-indigo	67

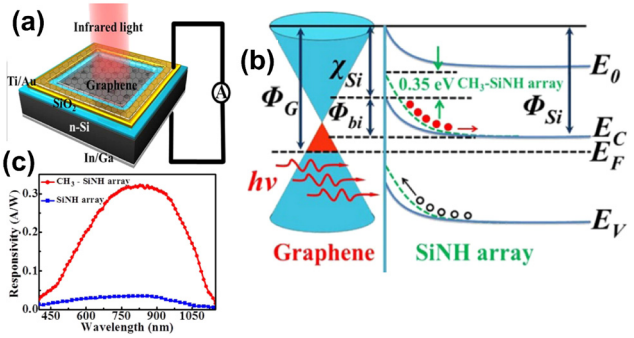

Fig. 14 (a) Schematic of a graphene/Si nanohole array Schottky junction based self-powered near-infrared photodetector, (b) energy band diagram of the device with and without surface passivation under light, and (c) responsivity with and without surface passivation for different wavelengths.[112] Published with "Optica Publishing Group" as open access, 2015.

9 Integrating additional effects

9.1 Pyro-phototronic effect

Pyroelectric materials exhibit the unique characteristic of generating a transient voltage across their surface in response to a temperature gradient. Incorporating pyroelectric materials into a self-powered photodetector makes it more efficient by supporting the existing built-in electric field. When light falls on a photodetector, the combined effect of the built-in electric field and the electric field due to pyroelectric materials results in a stronger electric field, which leads to an increase in the photocurrent. The complete process of e–h generation due to incident photons and separation of e–h pairs under the influence of a combined electric field is called the pyro-phototronic effect. A schematic of the pyro-phototronic effect is shown in Fig. 15, indicating that the pyro-phototronic effect is the combination of a semiconductor, photoexcitation, and pyroelectricity. The pyroelectric effect is observed in non-centrosymmetric materials. The pyroelectric effect is observed in materials such as ZnO, CdSe, a perovskite, SnS, crystalline rubrene, and several others.[116,117] The pyroelectric current flows through the device when light is illuminated and can be written as:[118]

$$J_{py} = \rho \frac{dT}{dt} \quad (18)$$

where J_{py} is the pyroelectric current density, ρ is the pyroelectric coefficient, and dT/dt gives the rate of change of temperature. The pyroelectric potential corresponding to the above current can be written in terms of equivalent device capacitance (C) as:[119]

$$dV_{py} = \rho A \frac{dT}{C} \quad (19)$$

There are four stages involved in the pyro-phototronic effect that occur during one period of light being turned ON and OFF.[115,120,121] These stages are also reflected in the transient response of the self-powered device, as demonstrated in Fig. 16.

- *1st stage*: the initial stage of the pyro-phototronic effect involves the incidence of light on the semiconductor surface, which generates a temperature gradient. The duration of this gradient is brief, but it results in a net electric displacement due to the redistribution of charges on the surface. As a result, a temporary electric potential, known as pyro-potential, develops across the device, which is additive to the built-in potential. This leads to an increase in the resulting potential difference across the device, causing the movement of photogenerated charge carriers more efficiently toward the electrodes. The total current consists of two components: the photocurrent (I_{ph}) due to the built-in electric potential and the pyro-

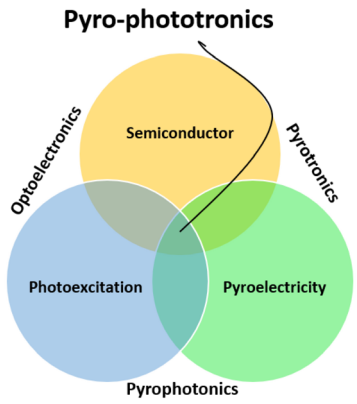

Fig. 15 Schematic diagram of the pyro-phototronic effect.[114]

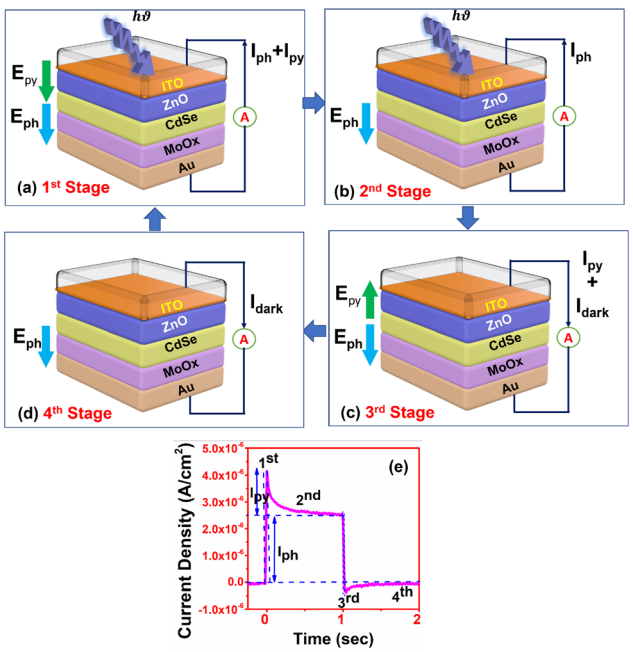

Fig. 16 (a–d) Four stages of pyro-phototronic effect, and (e) time response, of an ITO/ZnO QD/CdSe QD/MoO_x/Au-based self-powered photodetector.[115]

current (I_{py}) due to the pyro-potential. This stage is indicated as the 1st stage in Fig. 16(a) and (e).

• *2nd stage*: after a short period, the temperature gradient will start to decrease, causing a reduction in the pyro-current as indicated by eqn (18). As a result, the net effect on the device photocurrent will be an exponential decay due to the reduction in I_{py}, and the net current will eventually saturate to a value equal to the photocurrent (I_{ph}). This stage is illustrated in Fig. 16(b) and (e) as the second stage.

• *3rd stage*: when the light is turned OFF abruptly, it results in a negative temperature gradient, which leads to the development of pyro-potential in the opposite direction to the built-in potential. This pyro-potential supports the recombination mechanism, reducing the carrier lifetime and causing a sudden decrease in current. This stage is illustrated as the third stage in Fig. 16(c) and (e).

• *4th stage*: once the negative temperature gradient diminishes, the device returns to its thermal equilibrium state, as shown in the fourth stage of Fig. 16(d) and (e).

The pyro-phototronic effect leads to improved figures of merit such as detectivity, response time, responsivity, and EQE.[116] Chen *et al.*[86] demonstrated a self-powered photodetector based on AZO/ZnO/graphene, which utilized the pyro-phototronic effect. The device shows a good transient response with a 32 ms rise/fall time and a reported responsivity of 50 μA W^{-1}. The pyro-phototronic effect was also employed by Boruah *et al.*[64] along with a carrier transport layer of PEDOT:PSS and an active layer of ZnO NRs to achieve an improved transient response. The fabricated device demonstrated a rise time of 28 ms and a fall time of 23 ms,[64] with an enhanced responsivity of 2.2254 mA W^{-1}. To enhance the temperature gradient across the pyroelectric thin film, researchers have explored the use of energy exchange from indirect bandgap semiconductors. Chen *et al.*[122] utilized a Si-substrate (indirect bandgap semiconductor) and ZnO NWs (pyroelectric material) to achieve this. They reported an improved transient response with a rise time of 15 μs and a fall time of 21 μs due to the enhanced pyro-phototronic effect. Rana *et al.*[121] demonstrated that the figures of merit of self-powered devices could be further improved by utilizing a 100% illumination area. They fabricated an FTO/ZnO/NiO/Ag NW-based device, which exhibited a rise and fall time of 3.92 μs each and an improved responsivity of 290 mA W^{-1}. Similarly, Silva *et al.*[120] utilized a 100% illumination area and fabricated an ITO/ZnO/SnO_x/Si/Al-based self-powered device with an excellent transient response as shown in Fig. 17. The device exhibited a rise time of 2 μs, a fall time of 3 μs, and a responsivity of 64.1 mA W^{-1}.

The effect of a nanostructured semiconductor is also studied to improve the pyro-phototronic effect. Nanostructures exhibit higher polarization than their bulk counterparts, as reported by Zhang *et al.*[124] For instance, GaN NWs show pyroelectric coefficients that are 4.6 times higher than bulk GaN; this is attributed to the small-scale effect.[125] Therefore, quantum dots are most suitable for tunable self-powered photodetectors that utilize the pyroelectric effect. Goel and Kumar[115] employed ZnO QDs and CdSe QDs in combination with MoO_x as the hole transport layer to fabricate their device. The resulting device exhibited a sensitivity of approximately 330, a FWHM of 57 nm, and an EQE of 3.79%. Recently, Qiao *et al.*[123] reported an ITO ZnO NW/Si-based device to depict the dependence of the pyro-phototronic effect on the NWs' length. In the same article, they reported an ITO/ZnO NWs/PEDOT:PSS/Ag-based device as shown in Fig. 18(a). The transient characteristics shown in Fig. 18(b) indicate the increase in the pyro-phototronic effect with decreasing NW length. The pyro-phototronic effect depends on many factors associated with the device, such as junction type, transport layer, and electrode.

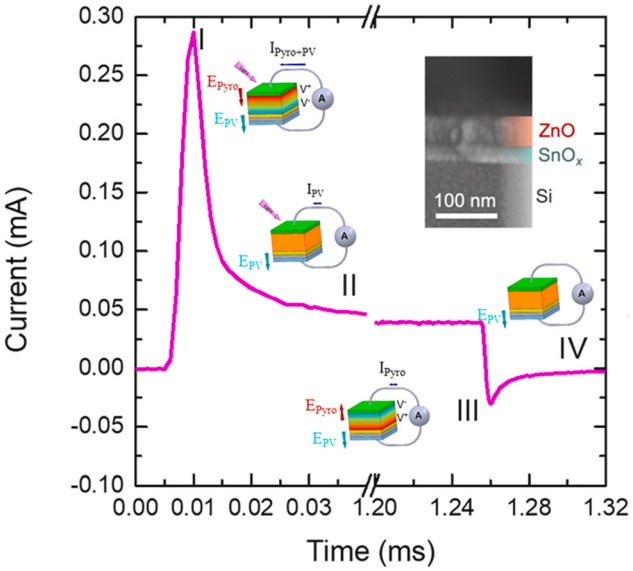

Fig. 17 Time response of an ITO/ZnO/SnO_x/Si/Al-based self-powered device with insets indicating four stages and a schematic.[120] Copyright "Elsevier", 2021 (included with permission).

• *Effect of a heterojunction*: Kumar *et al.*[92] developed a device based on an ITO/ZnO QDs/CdSe QDs/Au heterojunc-

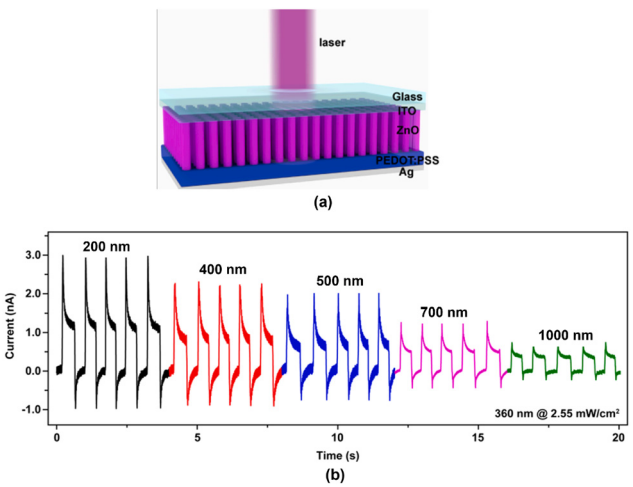

Fig. 18 (a) Schematic of an ITO/ZnO NW/PEDOT:PSS/Ag-based device. (b) Time response for different nanowire lengths.[123] Copyright "Elsevier", 2022 (included with permission).

tion, as depicted in Fig. 19(a). This device employs a heterojunction between CdSe and ZnO. Its transient response exhibits pyroelectric behavior with a pyroelectric current of 0.1 μA cm^{-2}, as demonstrated in Fig. 19(b). In addition, Kumar *et al.*[82] also fabricated a hybrid heterojunction device consisting of ITO/PQT-12/CdSe QDs/Au, as shown in Fig. 19(a). In contrast to ZnO QDs, PQT-12 is an organic polymer with pyroelectric properties. The pyroelectric current density in both devices is almost identical, as indicated in Fig. 19(b) and (c), although the PQT-12-based device has a lower overall current (*i.e.*, the sum of photocurrent and pyrocurrent) compared to the ZnO QD-based device due to the low mobility of organic materials. This PQT-12-based device has broad-spectrum coverage. Conversely, the ZnO QD-based device has narrowband detection capabilities, making it suitable for colour detection and image sensing applications.[4,12]

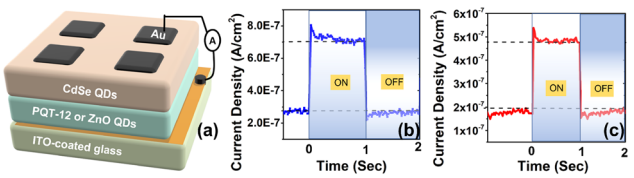

Fig. 19 (a) ITO/(ZnO QD, PQT-12)/CdSe QD/Au-based device, (b) transient response of ZnO QD-based device, and (c) transient response of PQT-12-based device under white light illumination.[82,92]

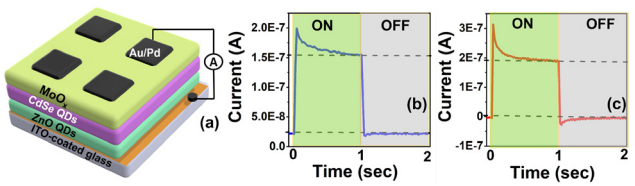

Fig. 20 (a) ITO/ZnO QD/CdSe QD/MoOx/(Pd,Au)-based device, (b) transient response of Pd-based device and (c) transient response of Au-based device under white light illumination.[92]

• *Effect of the transport layer*: as discussed earlier, the HTL plays a significant role in optoelectronic devices. In addition, the HTL can also impact the pyroelectric current in the device. Goel *et al.*[115] highlighted the advantages of incorporating the MoO_x layer as an HTL. They fabricated a device consisting of ITO/ZnO QDs/CdSe QDs/MoO_x/Au and compared its performance with the reported device that did not use MoO_x [92] while keeping all other layers the same. The results showed that the utilization of the MoO_x layer increased the pyroelectric current density from 0.1 μA cm^{-2} to 1.75 μA cm^{-2}. Hence, HTLs can also be employed to modify the pyroelectric response of the device.

• *Impact of electrodes*: a device's electrical and optical properties are significantly influenced by metal electrodes.[126] Kumar *et al.*[92] conducted a study to compare the performance of self-powered photodetectors comprising ITO/ZnO QDs/CdSe QDs/electrodes by changing the electrode material. They used Au and Pd as the electrodes and found that the device's performance could be enhanced by selecting the appropriate electrode. From the transient response of the devices, it was observed that the pyroelectric behavior was noticeable only in Au-based devices, with a pyroelectric current of 0.1 μA cm^{-2}, even though the device structures were similar. Goel and Kumar[53] fabricated an ITO/ZnO QDs/CdSe QDs/MoO_x/Pd-based device, as shown in Fig. 20(a), which showed little pyroelectric behaviour, with a pyroelectric current density of 0.587 μA cm^{-2}, as shown in Fig. 20(b). They also reported a device based on ITO/ZnO QDs/CdSe QDs/MoO_x/Au, similar to the previous structure, but with a change in the electrode material, as shown in Fig. 20(a). This device showed a pyroelectric current density of 1.75 μA cm^{-2}, as shown in Fig. 20(c). Therefore, it can be concluded that the pyroelectric behaviour is dominant in Au electrode-based devices compared to Pd electrode-based devices.

A list of different devices utilizing the pyro-phototronic effect is given in Table 6.

Table 6 Summary of different devices utilizing the pyro-phototronic effect

Structure	I_{ph} (nA)	I_{py} (nA)	Rise time (ms)	Fall time (ms)	Detectivity (Jones)	Responsivity (mA W^{-1})	EQE (%)	FWHM (nm)
FTO/ZnO/$MAPbI_3$/spiro-OMeTAD/Cu[127]	1500	1250	0.053	0.063	4.50×10^{10}	—	—	—
ITO/ZnO NW/p-Si/Cu[128]	350	800	1.2	1.3	1.40×10^{9}	13	—	—
FTO/ZnO NW/$MAPbI_3$/spiro-OMeTAD/Cu[129]	200	300	0.01	—	—	—	—	—
Al-ZnO NR/NiO/Si[130]	100	200	—	—	—	—	—	—
ITO/Cl:ZnO NW/PEDOT PSS/Ag[64]	220	344	28	23	1.54×10^{10}	2.2254	0.792	<100
PET/ITO/ZnO/Ag[131]	5	70	4.5	3.5	2.70×10^{9}	1.25	—	—
FTO/ZnO/p-NiO/Ag NW[121]	100 000	400 000	0.00392	0.0089	2.75×10^{11}	290	—	—
ITO/ZnO/ZnTe/Al[132]	500	3500	0.062	0.109	3.47×10^{12}	196.24	—	>100
AZO/ZnO/graphene[86]	200	2200	32	32	—	0.05	—	—
ITO/ZnO/p-Si/Ag[133]	1100	400	0.6	0.5	24.6×10^{9}	79.9	—	—
ITO/ZnO NW/p-Si/Cu[119]	780	4670	0.015	0.021	8.78×10^{11}	164	—	>100
n-Si/ZnO NW/PEDOT:PSS[134]	100	1400	—	—	—	22.054	—	—
ITO/ZnO/SnO_x/Si/Al[17]	50 000	250 000	0.002	0.003	2.40×10^{11}	64.1	—	>100
Cr/Au/BTO/p-GaN/Au/Cr[135]	560 000	670 000	160	235	—	—	—	—
ITO/ZnO/Si[123]	1.5	2	—	—	2.44×10^{11}	0.565	—	—
ITO/ZnO QDs/CdSe QDs/MoO_x/Au[115]	187.5	131.25	9.69	15.66	1.77×10^{10}	12.2	3.79	57
FTO/CQDs-ZNO NR/PEDOS/FTO[136]	30	30	78	77	5.00×10^{10}	10	—	—

9.2 Piezo-phototronic effect

Pyroelectric and piezoelectric behavior can be observed in 10 out of 32 crystal structures, particularly those with a wurtzite structure such as ZnO, CdSe, InN, and GaN. These materials exhibit anisotropic behaviour in various directions, resulting in piezoelectricity. In self-powered photodetectors, mechanical stress and strain can be utilized to modulate charge carrier generation, separation, extraction, and recombination phenomena. The piezoelectric effect in materials generates an electrical potential when subjected to mechanical stress. When combined with the photovoltaic effect caused by incident photons, this phenomenon is referred to as the piezo-phototronic effect. A schematic of the piezo-phototronic effect is shown in Fig. 21, indicating that the piezo-phototronic effect as the combination of a semiconductor, photoexcitation, and piezoelectricity. This effect is particularly useful for flexible, wearable self-powered devices, as it has been shown to improve performance by up to 70%.[139] Two-dimensional atomically thin materials and one-dimensional wurtzite NWs are ideal for flexible device fabrication as they can withstand significant strain.[79] Zhang *et al.*[138] fabricated a ZnO NRA-based self-powered photodetector that incorporated the piezo-phototronic effect, as illustrated in Fig. 22. When subjected to compressive strain, the detector's responsivity increased by approximately 2.75 times compared to when no strain was applied. Zhang *et al.*[140] reported a flexible MoS_2 p–n junction-based photodiode. This device offered a performance improvement by 319% due to the piezo-phototronic effect. MoS_2 can be used along with ZnO and CuO for the preparation of a self-powered photodetector utilizing the piezo-phototronic effect.[141,142] Other effects like flexophototronic[143] and photogating[144] can also be used in conjunction with the piezo-phototronic effect in self-powered photodetectors.

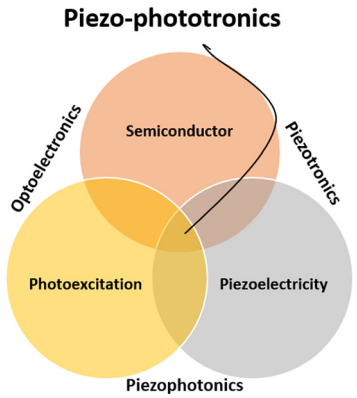

Fig. 21 Schematic of the piezo-phototronic effect.[137]

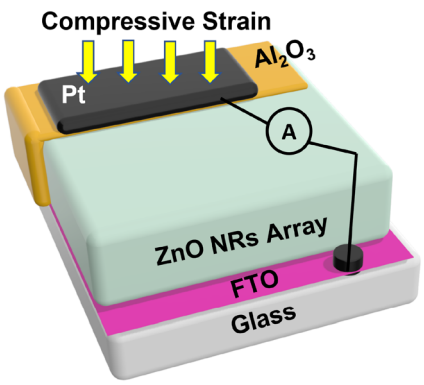

Fig. 22 Schematic of a self-powered photodetector utilizing the piezo-phototronic effect.[138]

9.3 Plasmonics

Metal nanoparticles can guide and confine light within a semiconductor by generating plasmons, which are oscillations of free electrons on the surface of the metal. These plasmons can interact with incoming light, enhancing the electric field near the surface of the solar cell/photodetector. The use of plasmonics has been shown to enhance the efficiency of photovoltaic devices significantly,[145,146] and it has also been applied to self-powered photodetectors. Plasmonics can be utilized in three ways:

1. *Front surface scattering*: plasmonic nanoparticles can be used on the device's front surface as shown in Fig. 23(a). This approach traps light by scattering the light within the semiconductor layer (absorber layer) when the wavelength of light is greater than the size of the metal nanoparticle. A point model described this phenomenon of light absorption and scattering. The scattering and absorption cross sections can be written as:[147]

$$C_{\text{scat}} = \frac{1}{6\pi}\left(\frac{2\pi}{\lambda}\right)^4 |\alpha|^2; \quad C_{\text{abs}} = \frac{2\pi}{\lambda}\text{Im}[\alpha] \tag{20}$$

where

$$\alpha = 3V\frac{\varepsilon_p/\varepsilon_m - 1}{\varepsilon_p/\varepsilon_m + 2} \tag{21}$$

where α, V, ε_p, and ε_m are the polarizability, particle volume, particle permittivity, and permittivity of the embedding medium, respectively. At $\varepsilon_p = -2\varepsilon_m$, the polarizability is maximal, known as surface plasmon resonance, at which the scattering cross-section is greater than the geometrical cross-section. It means for a small silver nanoparticle at resonance in air, the scattering cross-section is approximately ten times larger than its actual cross-sectional area. For light trapping, scattering should be more efficient than absorption. Catchpole

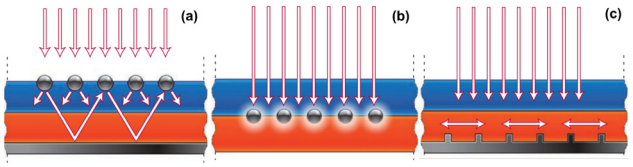

Fig. 23 Illustration of (a) front surface scattering, (b) sub-wavelength antenna, and (c) back surface corrugation.[146] Copyright "Nature Publishing Group", 2010 (included with permission).

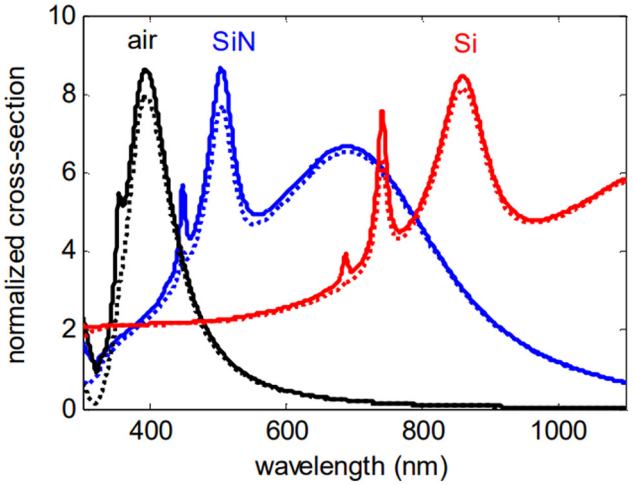

Fig. 24 Variation of scattering (dashed) and absorption cross-section (solid) of Ag-plasmonic nanoparticle embedded in different media.[147] Published with "Optica Publishing Group" as open access, 2008.

et al.[147] studied the effect of different embedding media on the scattering and absorption cross-section as shown in Fig. 24. It has been shown that there is spectral tuning with a change in the embedding medium, with air medium showing a peak in the UV region, SiN medium showing a peak in the visible region, and Si medium showing a peak in the infrared region. Sørensen *et al.*[148] studied the effect of the medium on the optical response. It has been found that there is a direct correlation between the refractive index and the amplitude of the plasmon resonance. The plasmon resonance amplitude gets intensified with an enhancement in the refractive index.

2. *Sub-wavelength antenna*: metallic nanoparticles are used as sub-wavelength antennas where the plasmonic near field and semiconductor are coupled and hence increase the effective absorption cross-section width as shown in Fig. 23(b). The efficiency of solar energy harvesting through nanoantennas heavily relies on their radiation efficiency.[149] The radiation efficiency is directly influenced by the type of metal used as a conductor and the size of the nanoantenna. The total radiation efficiency can be written as:[150]

$$\eta_{\text{total}}^{\text{rad}} = \frac{\int_{\lambda_{\text{start}}}^{\lambda_{\text{stop}}} P_{\text{inc}}(\lambda)\eta^{\text{rad}}(\lambda)\,\mathrm{d}\lambda}{\int_{\lambda_{\text{start}}}^{\lambda_{\text{stop}}} P_{\text{inc}}(\lambda)\mathrm{d}\lambda} \tag{22}$$

where P_{inc} is the wavelength function for a black body and can be written as:

$$P_{\text{inc}}(\lambda) = \frac{2\pi hc^2}{\lambda^5}\frac{1}{e^{\frac{hc}{\lambda k_B T}} - 1} \tag{23}$$

where T and c are the absolute temperature of the surface of the Sun and the speed of light, respectively.

3. *Back surface corrugation*: corrugations are small, regularly spaced indentations or bumps added to the solar cell/photodetector's surface. These indentations scatter incoming light, causing it to travel a longer distance through the device and increasing the probability that it will be absorbed. A corrugated metal film is used at the back surface. This efficiently couples sunlight in the surface plasmon polariton at the metal–semiconductor junction and increases the effective absorption thickness[146] as shown in Fig. 23(c).

Light trapping is particularly noticeable at the peak of the plasmon resonance spectrum (the reflectance *versus* frequency plot obtained using surface plasmon resonance excitation). This effect can be further adjusted using a dielectric in the surrounding medium. For instance, when small gold or silver nanoparticles are in the air, their plasmon resonance occurs at 480 nm and 350 nm, respectively. However, by employing commonly used materials like SiO_2, Si_3N_4, or Si in the manufacturing of solar cells, it is possible to shift these plasmon resonances across a range of 500 nm to 1500 nm.[146] Plasmonics help to efficiently reduce the thickness of the active layer. By reducing the thickness, both its cost-effectiveness and electrical properties can be improved. This is because a decrease in thickness reduces the dark current and increases the open-circuit voltage. Additionally, carrier recombination is minimized when carriers only travel a short distance before being collected at the junction, resulting in a higher photocurrent. Yu *et al.*[153] fabricated a self-powered photodetector using βGa_2O_3/NiO and designed it for solar-blind applications. The authors investigated the potential of inducing a plasmonic effect with Pt nanoparticles. They found that by utilizing the Pt nanoparticles, the responsivity, EQE, and rise/decay time increased from 0.245 to 4.27 mA W^{-1}, 0.72 to 1.97%, and 12/8 to 4.6/7.6 ms, respectively. Dai *et al.*[151] fabricated a dual-band self-powered photodetector using surface plasmon polarization as shown in Fig. 25. In this device, Au nanoparticles have been patterned on the InSe nanosheets as shown in Fig. 25(b). This device can sense photons from the visible to NIR regions. At 0 V, this device has 369 and 244 mA W^{-1} responsivities at 365 and 685 nm wavelengths. Hussain *et al.*[152] fabricated a plasma polymerized aniline-TiN (PPATiN) based broadband photodetector as shown in Fig. 26. This device shows enhanced figures of merit at low-intensity irradiance of 3.5 mW cm^{-2}. The responsivity of the device is 570 mA W^{-1} at zero bias. Lu *et al.* fabricated an Ag NP-based graphene/GaAs heterojunction. They just spun the layer of Ag nanoparticles onto the gra-

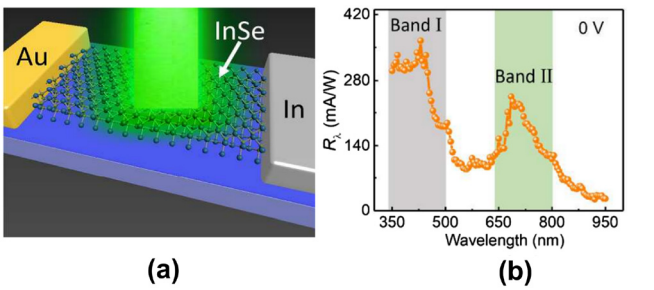

Fig. 25 (a) Schematic, and (b) responsivity *versus* wavelength of the plasmon-based InSe/Au dual-band self-powered photodetector.[151] Copyright "American Chemical Society", 2018 (included with permission).

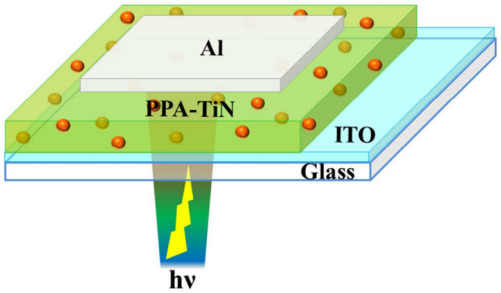

Fig. 26 Schematic of PPA-TiN-based hybrid photodetector.[152] Copyright "American Chemical Society", 2016 (included with permission).

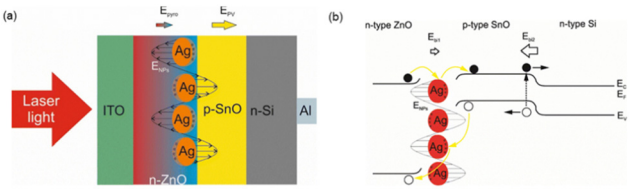

Fig. 27 (a) Schematic representation of synergistic effects, namely, photovoltaic, pyro-phototronic, and plasmonic in the Al/Si/SnO/Ag NP/ZnO/ITO device, and (b) energy band diagram.[154] Published with "Royal Society of Chemistry" as open access, 2024.

phene/GaAs surface and found exceptional results. The responsivity is increased by 38% while the detectivity is increased by 202%. This broadband device operates from 325 to 900 nm, peaking at ~405 nm.

Recently, Silva *et al.*[154] reported the tri-layered heterojunction of n-Si/p-SnO/n-ZnO as shown in Fig. 27(a). They incorporated a plasmonic effect utilizing Ag nanoparticles. The three synergistic effects, namely, photovoltaic, pyro-phototronic, and plasmonic, resulted in a responsivity of 210.2 mA W^{-1} and a rise (fall) time of 2.3 (51.3) μs. The energy band diagram in Fig. 27(b) indicates the development of a dual built-in electric field. However, the electric field developed due to the light-induced pyro-phototronic effect results in efficient carrier collection.

The utilization of polarization-sensitive materials results in improved figures of merit. Zhao *et al.* prepared a self-powered photodetector utilizing $MoSe_2$ and Te with a van der Waals heterojunction with a strong interlayer transition.[155] This device offered an extremely high detectivity in the order of ~10^{13} Jones and could be utilized to detect weak signals efficiently.

10 Perspective and summary

This review highlights the importance of adopting a suitable device engineering approach to improve the performance of self-powered photodetectors. It has been observed that the response time of a self-powered photodetector is higher than that of a conventional photodetector, which opens an area for researchers to investigate.

Material innovations may meet future requirements. The utilization of the perovskite QDs and 2D materials like MoS_2, $MoSe_2$, MXenes *etc.* could be the materials of choice. For example, flexible electronics will require a substrate with good mechanical strength, which can be achieved using 2D materials. The device with an organic material as an active layer requires a superior ETL and HTL. Spectrum selectivity can be improved by utilizing a good pyroelectric semiconducting material along with other novel functional materials with tunable band gap behaviour (colloidal QDs and 2D MXenes).

Several techniques can be utilized to enhance the performance of self-powered photodetectors, including ETL, HTL, bandgap and junction engineering and exploiting the piezo-phototronic and pyro-phototronic effects and plasmonics. These techniques hold significant potential for revolutionizing self-powered photodetectors, which are expected to play a vital role in future IoT networks and communication systems. Therefore, further research on these techniques could lead to significant advancements in the field of self-powered photodetectors. Moreover, mimicking the human eye's functioning is an exciting prospect for self-powered photodetectors. Researchers are exploring the possibility of developing self-powered photodetectors that mimic the human eye's structure and functioning, such as its high sensitivity and dynamic range. This could lead to the development of artificial vision systems that can detect, process, and respond to visual information without requiring external power sources. In addition, recent advancements in materials science and nanotechnology have enabled the development of novel materials and devices that can improve the efficiency and performance of self-powered photodetectors. For example, using 2D materials, such as graphene and transition metal dichalcogenides, has shown promising results in enhancing the photoresponsivity of self-powered photodetectors. Overall, the future of self-powered photodetectors looks promising. With further research and development, these devices can play a vital role in powering next-generation IoT networks, communication systems, and artificial vision systems.

Author contributions

Varun Goel: conceptualization, data curation, investigation, methodology, visualization, writing – original draft. Yogesh Kumar: formal analysis, funding acquisition, methodology, resources, validation, writing – review & editing. Gopal Rawat: funding acquisition, methodology, supervision, validation, writing – review & editing. Hemant Kumar: conceptualization, formal analysis, funding acquisition, investigation, methodology, resources, supervision, writing – review & editing.

Conflicts of interest

There are no conflicts to declare.

Acknowledgements

This work was supported in part by the Science and Engineering Research Board (SERB) through the Department of Science and Technology (DST), Government of India, under grant nos. SRG/2020/001282, EEQ/2022/000141, EEQ/2020/000183 and SRG/2020/000461.

References

1 J. J. Cadusch, J. Meng, B. J. Craig, V. R. Shrestha and K. B. Crozier, *Nanophotonics*, 2020, **9**, 3197–3208.
2 R. A. Dias, J. H. Correia and G. Minas, 2007 IEEE International Symposium on Industrial Electronics, 2007, pp. 2747–2751.
3 W. W. Moses, *Nucl. Instrum. Methods Phys. Res., Sect. A*, 2009, **610**, 11–15.
4 R. D. Jansen-van Vuuren, A. Armin, A. K. Pandey, P. L. Burn and P. Meredith, *Adv. Mater.*, 2016, **28**, 4766–4802.
5 F. Rutz, A. Bächle, R. Aidam, J. Niemasz, W. Bronner, A. Zibold and R. Rehm, *Infrared Technology and Applications XLV*, 2019, p. 1100211.
6 N. Martini, V. Koukou, G. Fountos, I. Valais, A. Bakas, K. Ninos, I. Kandarakis, G. Panayiotakis and C. Michail, *Procedia Struct. Integr.*, 2018, **10**, 326–332.
7 S. Liu, X. Zhang, X. Gu and D. Ming, *Biosens. Bioelectron.*, 2019, **143**, 111617.
8 C. Choi, M. K. Choi, S. Liu, M. Kim, O. K. Park, C. Im, J. Kim, X. Qin, G. J. Lee, K. W. Cho, M. Kim, E. Joh, J. Lee, D. Son, S.-H. Kwon, N. L. Jeon, Y. M. Song, N. Lu and D.-H. Kim, *Nat. Commun.*, 2017, **8**, 1–11.
9 C. I. Rablau, Fifteenth Conference on Education and Training in Optics and Photonics: ETOP 2019, 2019, pp. 1–14.
10 T. Mueller, F. Xia and P. Avouris, *Nat. Photonics*, 2010, **4**, 297–301.
11 M. Masoud, Y. Jaradat, A. Manasrah and I. Jannoud, *J. Sens.*, 2019, **2019**, 1–26.
12 Q. Lin, A. Armin, P. L. Burn and P. Meredith, *Nat. Photonics*, 2015, **9**, 687–694.
13 M. Peng, Y. Liu, A. Yu, Y. Zhang, C. Liu, J. Liu, W. Wu, K. Zhang, X. Shi, J. Kou, J. Zhai and Z. L. Wang, *ACS Nano*, 2015, **10**, 1572–1579.
14 A. Bera, A. D. Mahapatra, S. Mondal and D. Basak, *ACS Appl. Mater. Interfaces*, 2016, **8**, 34506–34512.
15 G. Rawat, D. Somvanshi, Y. Kumar, H. Kumar, C. Kumar and S. Jit, *IEEE Trans. Nanotechnol.*, 2016, 1–1.
16 H. Lu, W. Tian, F. Cao, Y. Ma, B. Gu and L. Li, *Adv. Funct. Mater.*, 2016, **26**, 1296–1302.
17 W. Tian, Y. Wang, L. Chen and L. Li, *Small*, 2017, **13**, 1701848.
18 W. Ouyang, J. Chen, Z. Shi and X. Fang, *Appl. Phys. Rev.*, 2021, **8**, 031315.
19 A. R. Jayakrishnan, J. P. Silva, K. Gwozdz, M. J. Gomes, R. L. Hoye and J. L. MacManus-Driscoll, *Nano Energy*, 2023, **118**, 108969.
20 M. F. Al Fattah, A. A. Khan, H. Anabestani, M. M. Rana, S. Rassel, J. Therrien and D. Ban, *Nanoscale*, 2021, **13**, 15526–15551.
21 C. Perumal Veeramalai, S. Feng, X. Zhang, S. V. N. Pammi, V. Pecunia and C. Li, *Photonics Res.*, 2021, **9**, 968.
22 R. Hui, *Introduction to Fiber-Optic Communications*, Elsevier, 2020, pp. 125–154.
23 B. N. Pal, I. Robel, A. Mohite, R. Laocharoensuk, D. J. Werder and V. I. Klimov, *Adv. Funct. Mater.*, 2012, **22**, 1741–1748.
24 J. Liu, M. Gao, J. Kim, Z. Zhou, D. S. Chung, H. Yin and L. Ye, *Mater. Today*, 2021, **51**, 475–503.
25 C.-T. Lee, T.-S. Lin and H.-Y. Lee, *IEEE Photonics Technol. Lett.*, 2010, **22**, 1117–1119.
26 M. Z. Nawaz, L. Xu, X. Zhou, K. H. Shah, J. Wang, B. Wu and C. Wang, *Mater. Adv.*, 2021, **2**, 6031–6038.
27 X. Zhang, M. Dai, W. Deng, Y. Zhang and Q. J. Wang, *Nanophotonics*, 2023, **12**, 607–618.
28 T. Kirchartz, J. Bisquert, I. Mora-Sero and G. Garcia-Belmonte, *Phys. Chem. Chem. Phys.*, 2015, **17**, 4007–4014.
29 M. Ding, Z. Guo, X. Chen, X. Ma and L. Zhou, *Nanomaterials*, 2020, **10**, 362.
30 P. Zheng, J. Yang, Z. Wang, L. Wu, H. Sun, S. Chen, Y. Guo, H. Xia, S. P. Phang, E.-C. Wang, J. Stuckelberger, H. C. Sio, X. Zhang, D. Macdonald and H. Jin, *Cell Rep. Phys. Sci.*, 2021, **2**, 100603.
31 R. Sharma, *Heliyon*, 2019, **5**, e01965.
32 D. Yang, L. Zhang, H. Wang, Y. Wang, Z. Li, T. Song, C. Fu, S. Yang and B. Zou, *IEEE Photonics Technol. Lett.*, 2015, **27**, 233–236.
33 M. D. Ward, W. Shi, N. Gasparini, J. Nelson, J. Wade and M. J. Fuchter, *J. Mater. Chem. C*, 2022, **10**, 10452–10463.
34 A. P. Singh, R. K. Upadhyay and S. Jit, *IEEE Trans. Electron Devices*, 2022, **69**, 3230–3235.
35 B. G. Streetman and S. Banerjee, *Solid State Electronic Devices*, Pearson, 7th edn, 2017.
36 D. K. Jarwal, C. Dubey, K. Baral, A. Bera and G. Rawat, *IEEE Trans. Electron Devices*, 2022, **69**, 5012–5020.
37 P. K. Mishra, S. Ayaz, T. Srivastava, S. Tiwari, R. Meena, B. Kissinquinker, S. Biring and S. Sen, *J. Mater. Sci.: Mater. Electron.*, 2019, **30**, 18686–18695.
38 D. Somvanshi, D. Chauhan, A. G. U. Perera, L. Li, L. Chen and E. H. Linfield, *IEEE Sens. Lett.*, 2019, **3**, 1–4.
39 V. Goel and H. Kumar, *IEEE Photonics Technol. Lett.*, 2023, **35**, 911–914.
40 N. Yamada, Y. Kondo, X. Cao and Y. Nakano, *Appl. Mater. Today*, 2019, **15**, 153–162.
41 A. V. Babichev, H. Zhang, P. Lavenus, F. H. Julien, A. Y. Egorov, Y. T. Lin, L. W. Tu and M. Tchernycheva, *Appl. Phys. Lett.*, 2013, **103**, 201103.
42 D. Bera, L. Qian, T.-K. Tseng and P. H. Holloway, *Materials*, 2010, **3**, 2260–2345.
43 C. Giansante, *Chem. – Eur. J.*, 2021, **27**, 14358–14368.

44 A. P. Alivisatos, *Science*, 1996, **271**, 933–937.
45 Y.-Q. Bie, Z.-M. Liao, H.-Z. Zhang, G.-R. Li, Y. Ye, Y.-B. Zhou, J. Xu, Z.-X. Qin, L. Dai and D.-P. Yu, *Adv. Mater.*, 2010, **23**, 649–653.
46 X. X. Liu and J. R. Sites, *J. Appl. Phys.*, 1994, **75**, 577–581.
47 S. Xu, Y. Qin, C. Xu, Y. Wei, R. Yang and Z. L. Wang, *Nat. Nanotechnol.*, 2010, **5**, 366–373.
48 W. Wu, S. Bai, M. Yuan, Y. Qin, Z. L. Wang and T. Jing, *ACS Nano*, 2012, **6**, 6231–6235.
49 J. Xu and G. Shen, *Nano Energy*, 2015, **13**, 131–139.
50 D. A. Neamen, *Semiconductor physics and devices: basic principles*, McGraw-Hill, New York, NY, 4th edn, 2012.
51 Y. Xie, L. Wei, Q. Li, G. Wei, D. Wang, Y. Chen, J. Jiao, S. Yan, G. Liu and L. Mei, *Appl. Phys. Lett.*, 2013, **103**, 261109.
52 H. Kumar, Y. Kumar, B. Mukherjee, G. Rawat, C. Kumar, B. N. Pal and S. Jit, *IEEE J. Quantum Electron.*, 2017, **53**, 1–8.
53 V. Goel and H. Kumar, *IEEE Photonics Technol. Lett.*, 2022, **34**, 1273–1276.
54 K. Shen, H. Xu, X. Li, J. Guo, S. Sathasivam, M. Wang, A. Ren, K. L. Choy, I. P. Parkin, Z. Guo and J. Wu, *Adv. Mater.*, 2020, **32**, 2000004.
55 H. Zhou, L. Yang, P. Gui, C. R. Grice, Z. Song, H. Wang and G. Fang, *Sol. Energy Mater. Sol. Cells*, 2019, **193**, 246–252.
56 Y. Li, H. Chen and J. Zhang, *Nanomaterials*, 2021, **11**, 1404.
57 E. Voroshazi, I. Cardinaletti, G. Uytterhoeven, A. Hadipour, B. P. Rand and T. Aernouts, 2013 IEEE 39th Photovoltaic Specialists Conference (PVSC), 2013, pp. 3212–3215.
58 T. Edvinsson, *R. Soc. Open Sci.*, 2018, **5**, 180387.
59 H. Kumar, Y. Kumar, G. Rawat, C. Kumar, B. Mukherjee, B. N. Pal and S. Jit, *IEEE Trans. Nanotechnol.*, 2017, **16**, 1073–1080.
60 L. Hu and A. Mandelis, *J. Appl. Phys.*, 2021, **129**, 091101.
61 C. B. Murray, D. J. Norris and M. G. Bawendi, *J. Am. Chem. Soc.*, 1993, **115**, 8706–8715.
62 C. J. Murphy, *Anal. Chem.*, 2002, **74**, 520 A–526 A.
63 R. H. Gilmore, E. M. Y. Lee, M. C. Weidman, A. P. Willard and W. A. Tisdale, *Nano Lett.*, 2017, **17**, 893–901.
64 B. D. Boruah, S. N. Majji, S. Nandi and A. Misra, *Nanoscale*, 2018, **10**, 3451–3459.
65 F. Abbasi, F. Zahedi and M. hasan Yousefi, *J. Mater. Sci.: Mater. Electron.*, 2021, **32**, 19614–19625.
66 K. D. A. Kumar, P. Mele, S. Golovynskyi, A. Khan, A. M. El-Toni, A. A. Ansari, R. K. Gupta, H. Ghaithan, S. AlFaify and P. Murahari, *J. Alloys Compd.*, 2022, **892**, 160801.
67 D. Alonso-Álvarez, T. Wilson, P. Pearce, M. Führer, D. Farrell and N. Ekins-Daukes, *J. Comput. Electron.*, 2018, **17**, 1099–1123.
68 D. P. Joseph and C. Venkateswaran, *J. At., Mol., Opt. Phys.*, 2011, **2011**, 1–7.
69 C.-Z. Ning, L. Dou and P. Yang, *Nat. Rev. Mater.*, 2017, **2**, 17070.
70 D. Singh, N. Singh, S. D. Sharma, C. Kant, C. P. Sharma, R. R. Pandey and K. K. Saini, *J. Sol-Gel Sci. Technol.*, 2010, **58**, 269–276.
71 Q. Hao, H. Yi, J. Liu, Y. Wang, J. Chen, X. Yin, C. S. Tang, D. Qi, H. Gan, A. T. S. Wee, Y. Chai and W. Zhang, *Adv. Opt. Mater.*, 2022, **10**, 2200063.
72 M. Yu, F. Gao, Y. Hu, L. Wang, P. Hu and W. Feng, *J. Colloid Interface Sci.*, 2020, **565**, 239–244.
73 S. Ebrahimi and B. Yarmand, *J. Alloys Compd.*, 2020, **827**, 154246.
74 E. Delli, V. Letka, P. D. Hodgson, E. Repiso, J. P. Hayton, A. P. Craig, Q. Lu, R. Beanland, A. Krier, A. R. J. Marshall and P. J. Carrington, *ACS Photonics*, 2019, **6**, 538–544.
75 F. Capasso, *Physica B+C*, 1985, **129**, 92–106.
76 F. Li, Y. Meng, R. Dong, S. Yip, C. Lan, X. Kang, F. Wang, K. S. Chan and J. C. Ho, *ACS Nano*, 2019, **13**, 12042–12051.
77 V. Goel and H. Kumar, in *Self-Powered Photodetectors: Fundamentals and Recent Advancements*, Bentham Science Publishers, 2023, pp. 256–291.
78 H. Shen, C. X. Shan, B. H. Li, B. Xuan and D. Z. Shen, *Appl. Phys. Lett.*, 2013, **103**, 232112.
79 X. Hu, X. Li, G. Li, T. Ji, F. Ai, J. Wu, E. Ha and J. Hu, *Adv. Funct. Mater.*, 2021, **31**, 2011284.
80 J. J. Hassan, M. A. Mahdi, S. J. Kasim, N. M. Ahmed, H. A. Hassan and Z. Hassan, *Appl. Phys. Lett.*, 2012, **101**, 261108.
81 V. Goel and H. Kumar, 2023 International Conference on Recent Advances in Electrical, Electronics & Digital Healthcare Technologies (REEDCON), 2023, pp. 47–49.
82 H. Kumar, Y. Kumar, G. Rawat, C. Kumar, B. Mukherjee, B. N. Pal and S. Jit, *IEEE Photonics Technol. Lett.*, 2017, **29**, 1715–1718.
83 K. Li, Y. Lu, X. Yang, L. Fu, J. He, X. Lin, J. Zheng, S. Lu, C. Chen and J. Tang, *InfoMat*, 2021, **3**, 1145–1153.
84 B. D. Boruah, A. Mukherjee and A. Misra, *Nanotechnology*, 2016, **27**, 095205.
85 L. Duan, F. He, Y. Tian, B. Sun, J. Fan, X. Yu, L. Ni, Y. Zhang, Y. Chen and W. Zhang, *ACS Appl. Mater. Interfaces*, 2017, **9**, 8161–8168.
86 D. Chen, Y. Xin, B. Lu, X. Pan, J. Huang, H. He and Z. Ye, *Appl. Surf. Sci.*, 2020, **529**, 147087.
87 H.-Y. Chen, K.-W. Liu, X. Chen, Z.-Z. Zhang, M.-M. Fan, M.-M. Jiang, X.-H. Xie, H.-F. Zhao and D.-Z. Shen, *J. Mater. Chem. C*, 2014, **2**, 9689–9694.
88 M. Mishra, A. Gundimeda, T. Garg, A. Dash, S. Das, Vandana and G. Gupta, *Appl. Surf. Sci.*, 2019, **478**, 1081–1089.
89 K. Benyahia, F. Djeffal, H. Ferhati, A. Bendjerad, A. Benhaya and A. Saidi, *J. Alloys Compd.*, 2021, **859**, 158242.
90 Y. Purusothaman, N. R. Alluri, A. Chandrasekhar, V. Vivekananthan and S.-J. Kim, *J. Phys. Chem. C*, 2018, **122**, 12177–12184.
91 Y. Chang, L. Chen, J. Wang, W. Tian, W. Zhai and B. Wei, *J. Phys. Chem. C*, 2019, **123**, 21244–21251.
92 H. Kumar, Y. Kumar, B. Mukherjee, G. Rawat, C. Kumar, B. N. Pal and S. Jit, *IEEE Trans. Nanotechnol.*, 2019, **18**, 365–373.

93 S. M. Hatch, J. Briscoe and S. Dunn, *Adv. Mater.*, 2012, **25**, 867–871.
94 S. M. Hatch, J. Briscoe, A. Sapelkin, W. P. Gillin, J. B. Gilchrist, M. P. Ryan, S. Heutz and S. Dunn, *J. Appl. Phys.*, 2013, **113**, 204501.
95 G. Huang, P. Zhang and Z. Bai, *J. Alloys Compd.*, 2019, **776**, 346–352.
96 T. Guo, C. Ling, X. Li, X. Qiao, X. Li, Y. Yin, Y. Xiong, L. Zhu, K. Yan and Q. Xue, *J. Mater. Chem. C*, 2019, **7**, 5172–5183.
97 P. Ghamgosar, F. Rigoni, M. G. Kohan, S. You, E. A. Morales, R. Mazzaro, V. Morandi, N. Almqvist, I. Concina and A. Vomiero, *ACS Appl. Mater. Interfaces*, 2019, **11**, 23454–23462.
98 R. Sinha, N. Roy and T. K. Mandal, *ACS Appl. Mater. Interfaces*, 2020, **12**, 33428–33438.
99 A. V. Agrawal, K. Kaur and M. Kumar, *Appl. Surf. Sci.*, 2020, **514**, 145901.
100 C.-Y. Huang, C.-P. Huang, H. Chen, S.-W. Pai, P.-J. Wang, X.-R. He and J.-C. Chen, *Vacuum*, 2020, **180**, 109619.
101 A. A. Ahmed, M. Hashim, T. F. Qahtan and M. Rashid, *Ceram. Int.*, 2022, **48**, 20078–20089.
102 X. Zhou, C. Wang, J. Luo, L. Zhang, F. Zhao and Q. Ke, *Chem. Eng. J.*, 2022, **450**, 136364.
103 R. Saha, A. Karmakar and S. Chattopadhyay, *Opt. Mater.*, 2020, **105**, 109928.
104 J. Jiang, J. Huang, Z. Ye, S. Ruan and Y.-J. Zeng, *Adv. Mater. Interfaces*, 2020, **7**, 2000882.
105 O. Game, U. Singh, T. Kumari, A. Banpurkar and S. Ogale, *Nanoscale*, 2014, **6**, 503–513.
106 S. Sarkar and D. Basak, *ACS Appl. Mater. Interfaces*, 2015, **7**, 16322–16329.
107 H. Chen, X. Sun, D. Yao, X. Xie, F. C. C. Ling and S. Su, *J. Phys. D: Appl. Phys.*, 2019, **52**, 505112.
108 C. Wei, J. Xu, S. Shi, Y. Bu, R. Cao, J. Chen, J. Xiang, X. Zhang and L. Li, *J. Colloid Interface Sci.*, 2020, **577**, 279–289.
109 W. Jin, Y. Ye, L. Gan, B. Yu, P. Wu, Y. Dai, H. Meng, X. Guo and L. Dai, *J. Mater. Chem.*, 2012, **22**, 2863.
110 Z. Gao, W. Jin, Y. Zhou, Y. Dai, B. Yu, C. Liu, W. Xu, Y. Li, H. Peng, Z. Liu and L. Dai, *Nanoscale*, 2013, **5**, 5576.
111 C. J. M. van Opdorp, PhD thesis, Applied Physics and Science Education, 1969.
112 L. Zeng, C. Xie, L. Tao, H. Long, C. Tang, Y. H. Tsang and J. Jie, *Opt. Express*, 2015, **23**, 4839.
113 L. Zhou, B. Bo, X. Yan, C. Wang, Y. Chi and X. Yang, *Crystals*, 2018, **8**, 226.
114 B. Ouyang, K. Zhang and Y. Yang, *iScience*, 2018, **1**, 16–23.
115 V. Goel and H. Kumar, *IEEE Trans. Electron Devices*, 2022, **69**, 6817–6824.
116 Q. Li, Z. Li and J. Meng, *Int. J. Optomechatronics*, 2022, **16**, 1–17.
117 S. K. Ghosh and D. Mandal, *Design strategy and innovation in piezo- and pyroelectric nanogenerators*, Elsevier, 2021, pp. 555–585.
118 J. C. Joshi and A. L. Dawar, *Phys. Status Solidi A*, 1982, **70**, 353–369.
119 L. Chen, J. Dong, M. He and X. Wang, *Beilstein J. Nanotechnol.*, 2020, **11**, 1623–1630.
120 J. P. Silva, E. M. Vieira, K. Gwozdz, A. Kaim, L. M. Goncalves, J. L. MacManus-Driscoll, R. L. Hoye and M. Pereira, *Nano Energy*, 2021, **89**, 106347.
121 A. K. Rana, M. Kumar, D.-K. Ban, C.-P. Wong, J. Yi and J. Kim, *Adv. Electron. Mater.*, 2019, **5**, 1900438.
122 L. Chen, B. Wang, J. Dong, F. Gao, H. Zheng, M. He and X. Wang, *Nano Energy*, 2020, **78**, 105260.
123 S. Qiao, H. Sun, J. Liu, G. Fu and S. Wang, *Nano Energy*, 2022, **95**, 107004.
124 J. Zhang, C. Wang, R. Chowdhury and S. Adhikari, *Scr. Mater.*, 2013, **68**, 627–630.
125 J. Zhang and C. Wang, *J. Appl. Phys.*, 2016, **119**, 145102.
126 V. Goel and H. Kumar, 2020 6th International Conference on Signal Processing and Communication (ICSC), 2020, pp. 243–247.
127 Z. Wang, R. Yu, C. Pan, Z. Li, J. Yang, F. Yi and Z. L. Wang, *Nat. Commun.*, 2015, **6**, 8401.
128 Z. Wang, R. Yu, X. Wang, W. Wu and Z. L. Wang, *Adv. Mater.*, 2016, **28**, 6880–6886.
129 W. Peng, R. Yu, X. Wang, Z. Wang, H. Zou, Y. He and Z. L. Wang, *Nano Res.*, 2016, **9**, 3695–3704.
130 B. Yin, H. Zhang, Y. Qiu, Y. Luo, Y. Zhao and L. Hu, *Nanoscale*, 2017, **9**, 17199–17206.
131 Y. Wang, L. Zhu, Y. Feng, Z. Wang and Z. L. Wang, *Adv. Funct. Mater.*, 2018, **29**, 1807111.
132 D. You, C. Xu, W. Zhang, J. Zhao, F. Qin and Z. Shi, *Nano Energy*, 2019, **62**, 310–318.
133 Y. Zhang, M. Hu and Z. Wang, *Nano Energy*, 2020, **71**, 104630.
134 W. Peng, Z. Pan, F. Li, Y. Cai and Y. He, *Nano Energy*, 2020, **78**, 105268.
135 Y. Zhang, J. Chen, L. Zhu and Z. L. Wang, *Nano Lett.*, 2021, **21**, 8808–8816.
136 N. Serkjan, X. Liu, T. Abdiryim, F. Liu, H. Zhang, A. Kadir, Y. Liu, X. Tang and Q. Cheng, *Carbon*, 2023, **204**, 387–397.
137 Z. L. Wang and W. Wu, *Natl. Sci. Rev.*, 2013, **1**, 62–90.
138 Z. Zhang, Q. Liao, Y. Yu, X. Wang and Y. Zhang, *Nano Energy*, 2014, **9**, 237–244.
139 L. Peng, L. Hu and X. Fang, *Adv. Funct. Mater.*, 2014, **24**, 2591–2610.
140 K. Zhang, J. Zhai and Z. L. Wang, *2D Mater.*, 2018, **5**, 035038.
141 K. Zhang, M. Peng, W. Wu, J. Guo, G. Gao, Y. Liu, J. Kou, R. Wen, Y. Lei, A. Yu, Y. Zhang, J. Zhai and Z. L. Wang, *Mater. Horiz.*, 2017, **4**, 274–280.
142 F. Xue, L. Chen, J. Chen, J. Liu, L. Wang, M. Chen, Y. Pang, X. Yang, G. Gao, J. Zhai and Z. L. Wang, *Adv. Mater.*, 2016, **28**, 3391–3398.
143 P. Guo, M. Jia, D. Guo, Z. L. Wang and J. Zhai, *Matter*, 2023, **6**, 537–553.
144 K. Zhang, M. Peng, A. Yu, Y. Fan, J. Zhai and Z. L. Wang, *Mater. Horiz.*, 2019, **6**, 826–833.

145 M. A. Green and S. Pillai, *Nat. Photonics*, 2012, **6**, 130–132.
146 H. A. Atwater and A. Polman, *Nat. Mater.*, 2010, **9**, 205–213.
147 K. Catchpole and A. Polman, *Opt. Express*, 2008, **16**, 21793–21800.
148 L. K. Sørensen, D. E. Khrennikov, V. S. Gerasimov, A. E. Ershov, S. P. Polyutov, S. V. Karpov and H. Ågren, *Phys. Chem. Chem. Phys.*, 2022, **24**, 24062–24075.
149 F. Duarte, J. P. N. Torres, A. Baptista and R. A. M. Lameirinhas, *Nanomaterials*, 2021, **11**, 422.
150 D. K. Kotter, S. D. Novack, W. D. Slafer and P. Pinhero, ASME 2008 2nd International Conference on Energy Sustainability, Volume 2, 2008, pp. 409–415.
151 M. Dai, H. Chen, R. Feng, W. Feng, Y. Hu, H. Yang, G. Liu, X. Chen, J. Zhang, C.-Y. Xu and P. Hu, *ACS Nano*, 2018, **12**, 8739–8747.
152 A. A. Hussain, B. Sharma, T. Barman and A. R. Pal, *ACS Appl. Mater. Interfaces*, 2016, **8**, 4258–4265.
153 J. Yu, M. Yu, Z. Wang, L. Yuan, Y. Huang, L. Zhang, Y. Zhang and R. Jia, *IEEE Trans. Electron Devices*, 2020, **67**, 3199–3204.
154 J. P. B. Silva, E. M. F. Vieira, K. Gwozdz, N. E. Silva, A. Kaim, M. C. Istrate, C. Ghica, J. H. Correia, M. Pereira, L. Marques, J. L. MacManus-Driscoll, R. L. Z. Hoye and M. J. M. Gomes, *Mater. Horiz.*, 2024, **11**, 803–812.
155 Q. Zhao, F. Gao, H. Chen, W. Gao, M. Xia, Y. Pan, H. Shi, S. Su, X. Fang and J. Li, *Mater. Horiz.*, 2021, **8**, 3113–3123.